



OPEN ACCESS

EDITED BY

Larry Lyons,
Department of Atmospheric and Oceanic
Sciences, College of Physical Sciences,
University of California, Los Angeles,
United States

REVIEWED BY

Jun Liang,
University of Calgary, Canada
Adolfo F. Vinas,
The Catholic University of America,
United States

*CORRESPONDENCE

J.-F. Ripoll,
✉ jean-francois.ripoll@cea.fr

SPECIALTY SECTION

This article was submitted
to Space Physics,
a section of the journal
Frontiers in Astronomy and Space
Sciences

RECEIVED 12 November 2022

ACCEPTED 06 February 2023

PUBLISHED 24 February 2023

CITATION

Ripoll J-F, Pierrard V, Cunningham GS,
Chu X, Sorathia KA, Hartley DP, Thaller SA,
Merkin VG, Delzanno GL, De Pascuale S
and Ukhorskiy AY (2023), Modeling of the
cold electron plasma density for radiation
belt physics.

Front. Astron. Space Sci. 10:1096595.
doi: 10.3389/fspas.2023.1096595

COPYRIGHT

© 2023 Ripoll, Pierrard, Cunningham,
Chu, Sorathia, Hartley, Thaller, Merkin,
Delzanno, De Pascuale and Ukhorskiy.
This is an open-access article distributed
under the terms of the [Creative
Commons Attribution License \(CC BY\)](https://creativecommons.org/licenses/by/4.0/).
The use, distribution or reproduction in
other forums is permitted, provided the
original author(s) and the copyright
owner(s) are credited and that the original
publication in this journal is cited, in
accordance with accepted academic
practice. No use, distribution or
reproduction is permitted which does not
comply with these terms.

Modeling of the cold electron plasma density for radiation belt physics

J.-F. Ripoll^{1,2*}, V. Pierrard^{3,4}, G. S. Cunningham⁵, X. Chu⁶,
K. A. Sorathia⁷, D. P. Hartley⁸, S. A. Thaller⁹, V. G. Merkin⁷,
G. L. Delzanno¹⁰, S. De Pascuale¹¹ and A. Y. Ukhorskiy⁷

¹CEA, DAM, DIF, Bruyeres-leChatel, France, ²UPS, CEA, LMCE, Bruyeres-leChatel, France, ³Royal Belgian Institute for Space Aeronomy, STCE and Space Physics, Brussels, Belgium, ⁴Université Catholique de Louvain (UCLouvain), Center for Space Radiations (CSR) and Georges Lemaître Centre for Earth and Climate Research (TECLIM), Earth and Life Institute (ELI), Louvain-La-Neuve, Belgium, ⁵Space Science and Applications Group, Los Alamos National Laboratory, Los Alamos, NM, United States, ⁶Laboratory for Atmospheric and Space Physics, University of Colorado, Boulder, CO, United States, ⁷Applied Physics Laboratory, Johns Hopkins University, Laurel, MD, United States, ⁸Department of Physics and Astronomy, University of Iowa, Iowa City, IA, United States, ⁹Orion Space Solutions, Louisville, CO, United States, ¹⁰Theoretical Division, Los Alamos National Laboratory, Los Alamos, NM, United States, ¹¹Oak Ridge National Laboratory, Oak Ridge, TN, United States

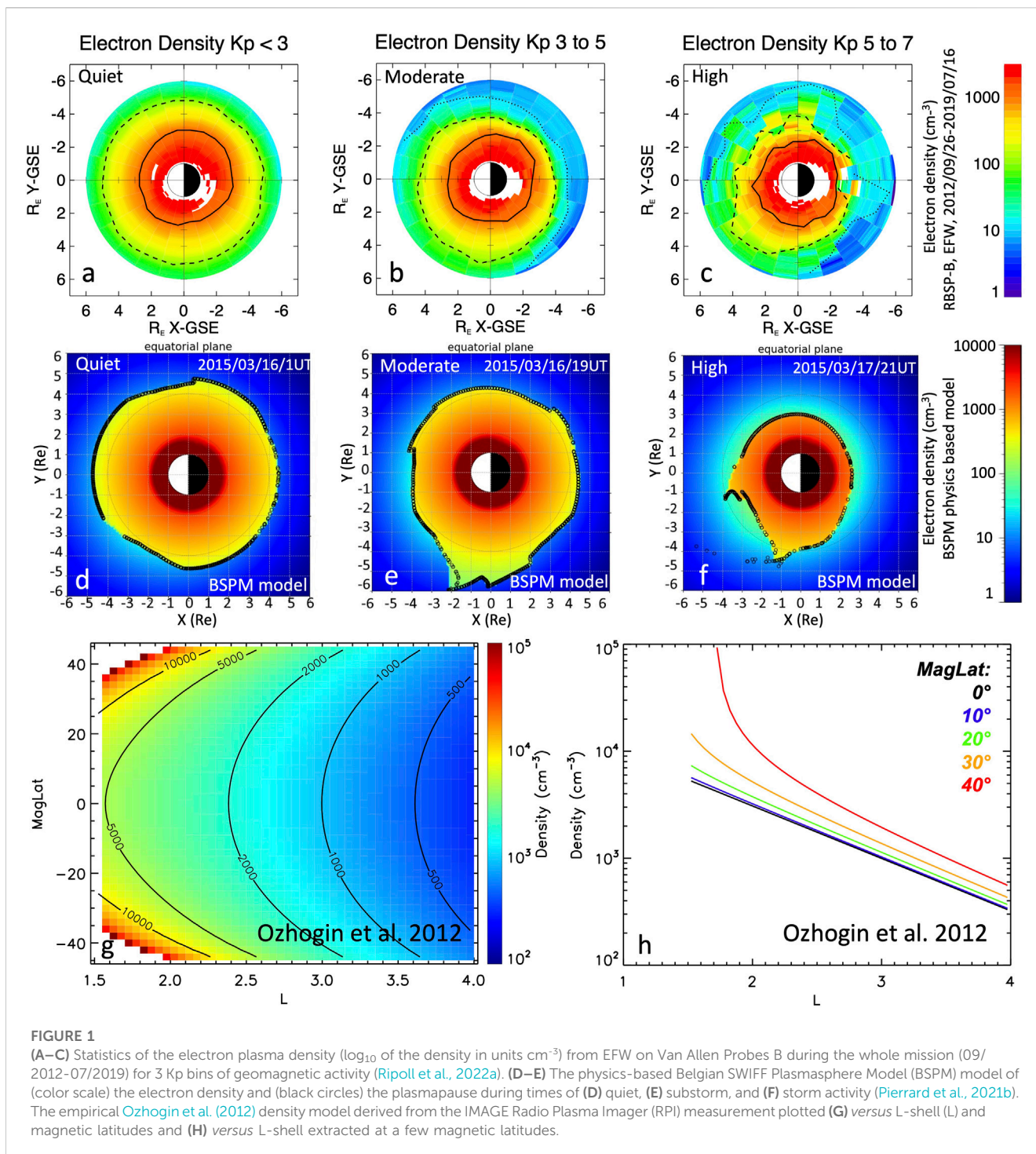
This review focusses strictly on existing plasma density models, including ionospheric source models, empirical density models, physics-based and machine-learning density models. This review is framed in the context of radiation belt physics and space weather codes. The review is limited to the most commonly used models or to models recently developed and promising. A great variety of conditions is considered such as the magnetic local time variation, geomagnetic conditions, ionospheric source regions, radial and latitudinal dependence, and collisional vs. collisionless conditions. These models can serve to complement satellite observations of the electron plasma density when data are lacking, are for most of them commonly used in radiation belt physics simulations, and can improve our understanding of the plasmasphere dynamics.

KEYWORDS

electron density, plasmasphere, plasmopause, empirical models, physical models, machine learning, radiation belts

1 Introduction

The Earth's plasmasphere is a region of cold (a few eV) plasma which originates from the ionosphere and forms a rotating torus that surrounds the Earth (Storey, 1953; Carpenter, 1963; Carpenter, 1966). Reviews of the plasmasphere can be found in Goldstein (2006), Kotova, 2007, Singh et al. (2011), Darrouzet and De Keyser (2013). For Earth's radiation belt codes computing the dynamics of energetic trapped electrons, accurate knowledge of the electron density over the entire plasmasphere is crucial for parameterizing the various diffusion coefficients (e.g., Glauert and Horne, 2005) used in modeling wave-particle interactions, either from a modeled density (e.g., Dahmen et al., 2022) or from local measurements (e.g., Ripoll et al., 2020b; Pierrard et al., 2021a). In addition, knowledge of the position of the outer edge of the plasmasphere is required for specifying a location to delineate between the high-density region where plasmaspheric hiss waves are present and the low-density region where chorus waves occur, with each wave causing different local loss



and acceleration processes through wave-particle interactions (Thorne, 2010). The ion compositions are undoubtedly also very important in radiation belt dynamics, for example, regarding the wave-particle interactions with electromagnetic ion cyclotron (EMIC) waves but this topic is not covered in this review. Authors interested in this topic can read the recent extended review of the known impact of the cold-ion and cold-electron populations in the Earth’s magnetosphere by Delzanno et al. (2021) with focus on the source of hot magnetospheric plasma,

solar-wind/magnetosphere coupling, magnetotail reconnection and substorms, Kelvin–Helmholtz instabilities on the magnetopause, wave-particle interactions, aurora structuring and spacecraft charging.

Figures 1A–C show statistics of the electron plasma density taken from Ripoll et al. (2022a) in which density is inferred from the Electric Field and Waves (EFW) spacecraft potential (Wygant et al., 2013) from Van Allen Probes B during the whole mission (09/2012–07/2019) (see more details about the method and the accuracy of the

cold plasma density in section 3.3). This figure illustrates the state of the plasmasphere for 3 bins in Kp index spanning quiet to high levels of geomagnetic activity, a range of conditions that models intend to reproduce. During quiet times, the plasmasphere is approximately circular in shape around the Earth, expanding out up to L-shell (L) of ~ 5.5 . With increasing activity, the plasmasphere evolves to become asymmetric in shape, with density structures forming in the morning and afternoon sectors. The increase of geomagnetic activity produces a general erosion of the plasmasphere on the dayside, an outward expansion of the plasma density in the dusk sector, and an increase of density in some of the night-morning sectors due to detached plasma regions rolling and wrapping around Earth.

In this article, we review existing plasma density models, including ionospheric source models, empirical density models, physics-based and machine-learning density models. A great variety of conditions is considered such as the magnetic local time (MLT) variation, geomagnetic conditions, ionospheric source regions, radial and latitudinal dependence, and collisional vs. collisionless conditions. This review is framed in the context of radiation belt physics (see review in Ripoll et al., 2020a) and space weather codes. This implies the models are usually derived to be applied on the large spatial scales and large temporal conditions. Models that will be referred to and discussed are limited to those most commonly used for radiation belt simulations. We also focus on the more recent progress made during the last decade and to the promising models or data, such as those from the National Aeronautics and Space Administration's (NASA) mission of the Van Allen Probes (Mauk et al., 2013). Models or data discussed in this review have gone through the calibration/correction analysis/process required to qualify the proper data to use (such as spacecraft potential correction, secondary electron effects, crosstalk effects correction in particle detectors, calibration corrections and modulation corrections on field detector antennae, etc.).

These models can be used to complement plasmaspheric densities inferred from satellite observations where or when data are lacking to fill data gaps, to be compared with these new data for evaluation, to be aggregated together or with observations to form more global models, or to analyze them for improving our understanding of the plasmasphere dynamics. Some of these models will serve as reference point or reference method from which we can improve and build a new generation of electron density models from the most recent observations, such as the NASA Van Allen Probes and the Japan Aerospace Exploration Agency (JAXA) Arase satellite missions (Miyoshi et al., 2018). The accuracy of the plasma density is essential for the computation of wave-particle interactions, which themselves determine the dynamics of the radiation belts.

2 The ionospheric source for the plasmasphere from the IRI model

The cold plasma in the plasmasphere has its origins in the ionosphere. Because the ionosphere is strongly driven by the Sun, the number density and temperature of the electrons, ions and neutrals in the ionosphere depend on solar activity, season, and local time, with a reset every day.

The earliest model of the topside ionosphere used only three bins in geomagnetic latitude and a linear dependence on F10.7 radio flux. In the 1990's, a diffusive equilibrium model was used to compute the density in the topside ionosphere. The diffusive equilibrium model is a first-principles model that specifies the plasma density along a flux tube given boundary conditions at the footpoints (Angerami and Thomas, 1964). The boundary conditions include the number density and temperature of electrons, ions and neutrals. A diffusive equilibrium model is applicable at low altitudes where collisions are frequent, but may have limited utility at higher altitudes where the plasma is collisionless.

The main empirical model of the ionosphere, the International Reference Ionosphere (IRI), uses trigonometric functions to fit both temporal (local, seasonal, and annual) and spatial variations in measurements of electron density coming from worldwide network of ionosondes, powerful incoherent scatter radars, topside sounders, and *in situ* instruments flown on many satellites and rockets, with the coefficients depending on solar activity. IRI has several altitude regions of interest: the D, E, F1, and F2 regions, and the topside ionosphere, which extends from the F2 peak to the maximum altitude in the model, 2000 km in IRI-2012 (Bilitza et al., 2014) (see also Bilitza et al., 2017; Bilitza, 2018). The IRI model is driven by several solar and ionospheric indices including the sunspot number R, the solar radio flux at 10.7 cm wavelength F10.7 (Tapping, 2013), and the ionosonde-based ionospheric global (IG) index (Bilitza, 2018). Last version is IRI 2020 on irimodel.org.

More specifically, the transition from highly collisional to collisionless in the topside ionosphere makes it a particularly difficult region to model. In IRI-2007, the topside ionosphere model from NeQuick (Coisson et al., 2006) was included as the default option. This model has been constructed from ISIS-2 topside sounder data orbiting at 1,400 km (see also Gulyaeva, 2012). Further extension to higher altitudes includes the work of Gulyaeva et al. (2002) who took available topside sounder profiles up to 3,500 km and built a connection of IRI to the bottom of the plasmasphere (IRI-PLAS) (see also Gulyaeva, 2011; Gulyaeva et al., 2011). Reinisch et al. (2007) also made an attempt to connect the IMAGE/RPI density data (see section 3.2) with IRI 2001 topside using the vary-Chap approach (see also discussion in Bilitza and Reinisch, 2008). This model was further improved in Nsumei et al. (2012).

3 Empirical models

3.1 Empirical plasma density models

Early efforts to model the plasmaspheric electron density included effects due to solar activity and season, with the first models providing the density using simple empirical relations depending on the McIlwain parameter L in Earth radii. Carpenter and Anderson (1992) derived a "reference profile" of the plasmaspheric electron density, valid for $2.25 < L < 8$, to describe the saturated plasmasphere, $N(L) = 10^{(-0.3145L+3.0943)}$, with additional dependences to include perturbations due to season and phase of the solar cycle. This model uses the International Sun-Earth Explorer (ISEE) measurements and is limited to the local time interval of

0–15 MLT omitting plasma expansion on the dusk side, which these authors had aimed to treat separately (Carpenter and Anderson, 1992). Lyons and Thorne (1973) used a form $N(L) = 1000(4/L)^4$, that was consistent with Carpenter et al. (1964), to derive electron lifetimes that yielded equilibrium flux profiles for $L = [1,5]$ using a Fokker-Planck radial diffusion code, even though the density model was not valid below $L = 2$. Albert (1999) used an exponential, $N(L) = 16400e^{-0.875L}$, instead of a power law in L . Sheeley et al. (2001) reported $N(L) = 1390(3/L)^{4.8} \pm 440(3/L)^{3.6}$ in the plasmasphere for $3 \leq L \leq 7$, where the authors show that the standard deviation captures differences between a newly filled and saturated plasmasphere. They did not find a magnetic local time (MLT) dependence for the plasmasphere, but did model the MLT-dependence of the plasma trough. A combination of Albert (1999) within the plasmasphere and Sheeley et al. (2001) within the plasma trough is used in the wave-particle interaction simulations of Ripoll et al. (2017) when satellite observations are lacking.

Gallagher et al. (2000) developed the Global Core Plasma Model (GCPM), a single unified model of the whole plasmasphere using an ‘amalgam’ of previously developed ‘region-specific’ models. GCPM addresses the density, temperature and composition of the plasmasphere, plasmopause, trough and polar cap. It depends on solar and geomagnetic indices, but is intended to be ‘representative’ of these conditions rather than used as a dynamic model. GCPM uses a modified version of the reference profile of Carpenter and Anderson (1992), $N(L) = 10^{-0.79L+5.3}$, added to the perturbations due to the solar cycle and season. It joins the topside ionosphere model of IRI to the equatorial plasma density model by first extrapolating the slope of the IRI model above the F2 peak using an exponential function and extrapolating the slope of the equatorial model downward in altitude with another exponential function, then blending the two functions with hyperbolic tangents. At higher latitudes, the shape of the exponential function is determined from IRI above the F2 peak, but the form is shifted by a constant so that the exponential decays to the equatorial value. The plasmopause location and width depend on local time. GCPM could be considered as the best compilation of all empirical density models. However, the GCPM model has not been directly coupled to radiation belt codes or wave particle interactions codes (to the knowledge of the authors) but it has been used for the validation of other plasma density models, themselves used in radiation belt codes (e.g., Ozhogin et al., 2012).

3.2 Latitudinal dependence

There have been recent efforts to model the variation of electron density with magnetic latitude. Denton et al. (2006) used satellite measurements from Polar and the Combined Release and Radiation Effects Satellite (CRRES) to model the latitudinal variations as a power law of the radial distance R to any point along the field line, $N(L, R) = N_{eq}(LR_E/R)^\alpha$, and fit α as a function of L and equatorial density for $L > 2$. Denton et al. (2006) fit this model to IMAGE RPI data and found that it did not perform well at high magnetic latitudes. Reinisch et al. (2004) and Huang et al. (2004) found that the following form fits data from IMAGE RPI well:

$$N(L, \lambda) = N_{eq}(L)[1 + \gamma\lambda/\lambda_{INV}][\cos((\pi/2)(\alpha\lambda/\lambda_{INV}))]^{-\beta} \quad (1)$$

where λ is the magnetic latitude, λ_{INV} is the invariant magnetic latitude, and the fitting parameters are α, β, γ . Ozhogin et al. (2012) built on the earlier work of Reinisch et al. (2004) and fixed the values of the fitting parameters to

$$\alpha = 1.01 \pm 0.03, \beta = 0.75 \pm 0.08, \gamma = 0 \text{ and} \quad (2)$$

$$N_{eq}(L) = 10^{-(0.4903 \pm 0.0315)L + (4.4693 \pm 0.0921)}$$

The Ozhogin et al. (2012) model is restricted to altitudes greater than 2000 km and $L > 1.5$, up to $L = 4$, and does not address dependence on MLT, season, solar activity, or differences in density between the Northern and Southern hemispheres. This model is plotted in Figures 1G, H to illustrate the increase of density with latitude. Models of Carpenter and Anderson (1992), Gallagher et al. (2000), Denton et al. (2006), Sheeley et al. (2001) and Ozhogin et al. (2012) are compared in Figure 8 of Ozhogin et al. (2012).

Empirical and first-principles models of the cold plasma density in the plasmasphere have been in development since the 1960’s, but there is just one model (Ozhogin et al., 2012) that is valid below $L = 2$ and includes latitudinal dependence. To our knowledge, there was no valid empirical model below $L = 1.5$, nor one that includes variations due to solar activity, season, local time, and hemispheric differences, in addition to L, λ below $L = 2$. Recently, Hartley et al. (2023) combined Van Allen Probes data for latitudes below 20° with Arase data up to 40° for $1 < L \leq 3$ and derived a new electron density model with both a latitudinal and MLT dependence. Comparison with the L dependence of the Ozhogin model shows good agreement above $L = 1.5$. Below $L = 1.5$, a fitting form similar to the Ozhogin model is adopted with new parameters defined as $\alpha = 1.03, \beta = 0.44$. An MLT dependence of the plasma density was identified, which is consistent with the diurnal variation of ionosphere. This variation is strongest at low L , but persists out to $L = 3$. All empirical electron density models discussed in this article are listed and succinctly synthesized in Table 1.

3.3 Empirical plasmopause models

There exist a variety of empirical plasmopause models currently used in radiation belt simulations. They generally provide the radial distance of the plasmopause in the equatorial plane as a simple function of the geomagnetic activity level. Tu et al. (2009) used, for instance, the CRRES data driven model of O’Brien and Moldwin (2003), whereas Tu et al. (2013) implemented the Carpenter and Anderson (1992) plasmopause model (noted CA92). The CA92 plasmopause model is the most commonly used model to our knowledge. It has been largely used for radiation belt studies over the last 10 years (Subbotin and Shprits, 2009; Kim et al., 2011; Shprits et al., 2013; Ripoll et al., 2016; Ripoll et al., 2019; Wang and Shprits, 2019; Cervantes et al., 2020a; Cervantes et al., 2020b; Malaspina et al., 2020; Saikin et al., 2021).

Recently, Ripoll et al. (2022a) derived both a plasmopause and a 100 #/cc density level models based on the entire Van Allen Probes mission (2012–2019) from both the Electric and Magnetic Field Instrument Suite and Integrated Science (EMFISIS) suite’s (Kletzing et al., 2013) and the Electric Field and Waves (EFW) (Wygant et al.,

TABLE 1 Empirical electron density models discussed in this article.

Name/Reference	Modeled quantity	Data in use (or type of physics)	Model validity domain	Known limitation
Carpenter and Anderson (1992)	Plasmasphere and plasma trough density with MLT dependence. Plasmopause	ISEE	valid for $2.25 < L < 8$	0 to 15 MLT. Underestimation of the plasmopause position shown in Ripoll et al. (2022a)
Lyons and Thorne (1973)	Density	Whistler measurements and OGO-5	$L = [1,5]$	Not valid below $L = 2$. Limited to within the plasmasphere
Albert (1999)	Density	ISEE	Based on Carpenter and Anderson (1992) averaged over MLT	Limited to within the plasmasphere
Sheeley et al. (2001)	Density with MLT dependence	CRRES	$3 \leq L \leq 7$	CRRES limitation in MLT and temporal coverage. Gap at high L shell between dawn and noon. No dependence on magnetic activity
Albert (1999) within the plasmasphere and Sheeley et al. (2001) within the plasma trough	Density	ISEE and CRRES	valid for $2.25 < L < 7$	Limitations of Carpenter and Anderson (1992) and Sheeley et al. (2001)
GCPM Gallagher et al. (2000)	3D Density, temperature and composition of the plasmasphere, plasmopause, trough and polar cap	Compilation of all empirical density models	L in $[1, 8]$	Not a dynamic model and only representative of typical conditions
Denton et al. (2004)	Density with MLT dependence	Polar	L in $[2, 8]$, $n_e < 1,500 \text{ #/cm}^{-3}$	Limited to March 1996 to September 1997
Denton et al. (2006)	Density with latitudinal dependence	Polar and CRRES	L in $[2, 8]$	Power law form to describe the field line distribution
Ozhogin et al. (2012)	Density with latitudinal dependence	IMAGE/RPI	altitudes greater than 2000 km and $L > 1.5$, up to $L = 4$	no MLT, season, solar activity, or differences between both hemispheres
Berube et al. (2005)	Equatorial density	IMAGE/RPI	L in 2–5	data between May 2000 and May 2001
Hartley et al. (2023)	Density with latitudinal and MLT dependences	Van Allen Probes data for latitudes below 20° with Arase data up to 40°	L in $[1,3]$. Continuous with Ozhogin et al. (2012) up to $L = 4$	Low L-shell model
Denton et al. (2012)	Long-term (>1 day) density refilling rates	IMAGE/RPI	L in $[2, 9]$	No MLT dependence of refilling rate. $K_p < 1.5$. 34 quiet periods of ~2 days between 2001 and the end of 2005

2013) data. The cold plasma densities are either determined by the upper hybrid resonance (UHR) method from EMFISIS measurements ([Kurth et al., 2015](#)) or by using the spacecraft floating potential ([Escoubet et al., 2007](#); [Torkar et al., 2016](#); [Torkar et al., 2019](#)) measured by the Electric Field and Waves (EFW) instrument ([Wygant et al., 2013](#)).

About the accuracy of these density measurements, we note the densities derived along with the corresponding spacecraft potentials are fit to a function with a non-linear least squares fit. The resulting fits typically have a Pearson (R^2) coefficient in the range of ~ 0.75 – 0.95 and an average percent error between the selected fit derived densities and the densities used to perform the fit of $\sim 15\%$. Experiments with individual orbits show that fits of the functional form can capture the density voltage relation over a range of densities from \sim few cm^{-3} up to $3,000 \text{ cm}^{-3}$ with the lower densities still agreeing with the EMFISIS UHR densities to within 10%. However, using the same fit for a longer period (larger than an orbit) the EFW and EMFISIS densities may diverge by over factor of two at densities $< 10 \text{ cm}^{-3}$. The reason for this is the variability of the plasma environment outside the plasmasphere. For periods during

which the upper hybrid resonance line is clearly resolved in the High Frequency Receiver (HFR) spectral data, the EMFISIS density product is generally more accurate than the EFW. However, during times in which there are high levels of wave activity that make identification of the upper hybrid line difficult or impossible, resulting in increased uncertainty in the EMFISIS densities, the EFW density fits still return densities by applying the relevant fit equation to the spacecraft potential. Regarding the semi-automated process for determining the EMFISIS density from the UHR ([Kurth et al., 2015](#)), there is a 8.7% mean percentage difference between the manual process and the semiautomatic process, which is less than the $\sim 10\%$ resolution available for an individual measurement. This difference is visible in Figure A2 of [Goldstein et al. \(2014a\)](#), where the average difference is often low ($\sim 7\%$), is less than 20% in general, but can be up to 100% for a very small number of data points. Another main source of error is the spectral resolution, due to the upper hybrid resonance that can only be defined at specific values dictated by the binned frequency spectrum. This translates to a density resolution of $\Delta n_e/n_e$ of about 10%. The uncertainty increases when the spectra become difficult to interpret,

TABLE 2 Empirical plasmopause models discussed in this article.

Name/ References	Modeled quantity	Data in use (or type of physics)	Model validity domain	Known limitation
O'Brien and Moldwin (2003)	Plasmopause with MLT dependence	CRRES	L in [2, 8]	CRRES limitation in MLT and temporal coverage. Gap at high L shell between dawn and noon
Ripoll et al. (2022a)	Plasmopause and 100 #/cc level line, with MLT dependence	Van Allen Probes	L in [1.5, 6]	Single index modeling
Kwon et al. (2015)	Plasmopause	THEMIS	Kp~1	Limited to quiet times
Bandić et al. (2016)	Plasmopause with MLT dependence	CRRES	L in [2, 8]	Sector (12–18 MLT) contains significantly less data than other sectors
Cho et al. (2015)	Plasmopause	THEMIS (2008–2012)	L in [2, 8]	Ascending phase of Solar Cycle 24. Sharper gradient than commonly used. No MLT dependence
Liu and Liu (2014)	Plasmopause with MLT dependence	THEMIS D (2010–2011)	L in [3, 6]	Generalized in Liu et al. (2015)
Liu et al. (2015)	Plasmopause with MLT dependence	THEMIS (2009–2013)	L in [2, 8]	Limited to plasmopause crossings with one sharp density gradient
Verbanac et al. (2015)	Plasmopause with MLT dependence	Cluster	L in [2.9, 8.8]	Limited to 311 plasmopause crossing
NSW-GDP Model He et al. (2017)	Plasmopause with MLT dependence	Multiple sources (18 satellites in 1977–2015). 48,899 plasmopause locations	L in [2, 8]	The maximum RMS error of 0.91 RE at 17 h MLT. Minimum RMSE of 0.57 RE at midnight. Diurnal plasmopause variations may be faded through 36 years data averaged in 1 h UT intervals

as discussed in Goldstein et al. (2014a). In most instances, the spectral resolution uncertainty is estimated to be between 10% and 20% (Hartley et al., 2016). The EMFISIS and EFW densities from $\sim 10 \text{ cm}^{-3}$ to $3,000 \text{ cm}^{-3}$ are statistically compared in Jahn et al. (2020), who found that the EFW values predominantly fall in a range of 50%–200% of their corresponding EMFISIS measured value (e.g., 0.5 to 2 times the actual value), while most of the EFW to EMFISIS points used for comparison are $\sim 100\%$ (e.g., $n_{\text{EFW}} \sim n_{\text{EMFISIS}}$). Further comparisons of the 100 #/cc level are carried out in Ripoll et al. (2022a) in which Figures 1K, L confirm the good agreement between both methods, with the bulk of normalized differences below $\pm 20\%$.

A comparison of the CA92 plasmopause model with Van Allen Probes measurements is performed in Ripoll et al. (2022a). These authors first recover the CA92 model using EMFISIS data and a gradient method to localize the plasmopause, showing the practical reliability of the CA92 model. However, direct comparisons of the 100 cm^{-3} level deduced from Van Allen Probes EFW measurements and the CA92 model show the dense plasmasphere expands farther out than predicted by the CA92 model. Departure of the CA92 model from the 100 cm^{-3} EFW data increases as the maximum value of the Kp index over the last 24 h (Kp) increases and L-shell decreases, and storm-induced erosions are less deep than predicted by the CA92 model (Ripoll et al., 2022a).

The model of O'Brien and Moldwin (2003) based on CRRES data is the first to show the MLT dependence as well as the relevance of parametrizing the plasmopause model with various indices, such as Kp, AE, and Dst (see also Moldwin et al. (2002)). Carpenter et al. (2000) states the experimental error in the CRRES density is associated with measuring the UHR or plasma frequencies on the

SFR records. They estimated to be $\pm 6\%$ in spectral resolution ($\Delta f/f$), which corresponds to $\pm 12\%$ in density. Kwon et al. (2015) derived the median/mean plasmopause locations from the electron density inferred from the Time History of Events and Macroscale Interactions during Substorms (THEMIS) spacecraft potential under steady quiet conditions ($Kp \leq 1$). The comparison of their plasmopause model with the estimated L_{pp} from models such as GCPM (Gallagher et al., 2000), Moldwin et al. (2002), and O'Brien and Moldwin (2003) with $Kp = 1$ shows the plasmopause is farther extended $\sim 1\text{--}2 L$ from the Earth (i.e., GCPM and CRESS based-models underestimate the extend of the plasmopause). Ripoll et al. (2022a) show the underestimation of the plasmopause position is caused by the gradient method that fails identifying gradients particularly during quiet times and on the dusk.

Other plasmopause models include Bandić et al. (2016) based on CRRES data, Cho et al. (2015), Liu and Liu (2014) and Liu et al. (2015) based on THEMIS data, and Larsen et al. (2007) based on IMAGE data. Verbanac et al. (2015) plasmopause model is based on CLUSTER data and analytical relationships obtained from geomagnetic and solar wind observations. Bandić et al. (2017) derived a plasmopause model from a large dataset including multiple sources. A comparison of these models is provided in Pierrard et al. (2021c) showing a great variability of mean plasmopause empirical models (see also Guo et al., 2021). All empirical plasmopause models discussed in this article are listed and succinctly synthesized in Table 2 (see also Table 1 in He et al. (2017) listing the model dependences).

The large variability of the measurements underlying the mean empirical plasmopause models (more generally mean plasma density empirical models) is one major limitation of this type of

models that calls for the use of either physic-based models or machine learning technics.

4 Physic-based models of the plasmasphere

4.1 Ionosphere-plasmasphere models

The 3D global ionosphere/plasmasphere fluid model SAMI3 (Huba and Krall, 2013; Krall and Huba, 2013) of the Naval Research Laboratory (NRL) solves the continuity and momentum fluid equations for seven ion species (H^+ , He^+ , N^+ , O^+ , N_2^+ , NO^+ and O_2^+) and includes the thermospheric wind-driven dynamo electric field. It is based on SAMI2 (Huba et al., 2000). SAMI3 uses the partial donor cell method (Hain, 1987; Huba, 2003) and a newly implemented 4-order flux-corrected transport scheme for ExB transport perpendicular to the magnetic field (Huba and Liu, 2020). The temperature equation is solved for three atomic ion species and electrons. The model has a co-rotation potential, a neutral wind dynamo potential (with winds from HWM93 (Hedin, 1987)), and a time-dependent Volland-Stern-Maynard-Chen potential. In Huba and Krall (2013), SAMI3 density results are compared at the equator for 4 MLT sectors with the quiet time empirical electron density of Berube et al. (2005) defined as $n_{eq} = 10^{0.51L+4.56}$ for L in 2–5 from IMAGE RPI data between May 2000 and May 2001. They find the SAMI3 electron density is lower by a factor 2 attributed to a lower F10.7 index used in the simulation.

The SAMI3 model has been recently modified to support the NASA ICON mission and provide ionosphere and thermosphere properties during this mission (Huba et al., 2017). SAMI3 recently integrated an improved model of counterstreaming H^+ outflows from the two hemispheres during storm using a two fluid species for H^+ (Krall and Huba, 2019) in order to avoid non-physical high-altitude ‘top-down refilling’ density peaks (Krall and Huba, 2021). SAMI3 is currently used to try to reproduce the formation of density ducts in the plasmasphere (e.g., Jacobson and Erickson, 1993; Loi et al., 2015) caused by the thermosphere composition and winds on plasmaspheric refilling outflows (Krall et al., 2018) as observed from the Murchison Widefield Array (MWA) interferometric radio telescope in Australia (Helmboldt and Hurley-Walker, 2020). SAMI3 recently coupled to the atmosphere/thermosphere code WACCM-X (Whole Atmosphere Community Climate Model with thermosphere and ionosphere extension) provided the first high-resolution global simulation using realistic thermospheric conditions of the formation and penetration of plasma bubbles into the topside F layer (Huba and Liu, 2020). These structures will further propagate to higher altitudes and introduce longitudinal and seasonal dependence structures into the plasmasphere. Further coupling of SAMI3 and applications are discussed in Huba (2023).

The Ionosphere-Plasmasphere-Electrodynamics (IPE) model is derived in Maruyama et al. (2016) to investigate the connection between terrestrial and space weather (e.g., Fuller-Rowell et al., 2008). IPE provides 3D thermal plasma densities for nine ion species, electron and ion temperatures, and parallel and perpendicular velocities of the ionosphere and plasmasphere. The parallel plasma transport is based on the Field Line Interhemispheric Plasma (FLIP) Model (Richards et al., 2010). There is a detailed

model of the Earth’s magnetic field using Apex coordinates (Richmond, 1995) and the International Geomagnetic Reference Field IGRF (as in SAMI3). The transport is computed with the same solver all the way from the equator to the pole on a global static grid with a semi-Lagrangian scheme that allows for the global plasma transport perpendicular to magnetic field lines. There is a self-consistent photoelectron calculation enabling more accurate studies of the longitudinal/UT dependence of the ionospheric mass loading process. IPE is generally defined from 90 km to approximately 10,000 km. The spatial resolution of the radial direction in the plasmasphere varies from $0.05 R_E$ ($L = 1.5$) to $0.46 R_E$ ($L = 5$). IPE has used to reproduce the Weddell Sea Anomaly (Sun et al., 2015) and for studying extreme plasmaspheric erosion as low as $L \sim 1.7$ (Obana et al., 2019). Current applications of IPE include plasmaspheric drainage plumes, ionospheric storm enhanced density (SED) plumes, plasmaspheric refilling, and plasmaspheric composition. The Whole Atmosphere Model (WAM)(e.g., Akmaev and Juang, 2008) has been coupled with IPE (WAM-IPE) and provides today space weather forecast 24/7 at NOAA SWPC (<https://www.swpc.noaa.gov/products/wam-ipe>). WAM-IPE has recently be used to simulate ESF irregularities (Hysell et al., 2022).

The IRAP Plasmasphere Ionosphere Model (IPIM) uses a 16-moment approach for strong temperature anisotropy at high altitude and for accurately modeling the transition between collision dominated at low altitude and collisionless media at high altitude (Marchaudon and Blelly, 2015). IPIM solves the interhemispheric hydrodynamics convection and corotation of six ions and thermal electrons along flux tubes at different distances from Earth. IPIM has a kinetic model for suprathermal electrons and solves for the chemical reactions in the ionosphere. IPIM has been used to simulate the depletion of the ionospheric F_2 layer by a high-speed stream for short-term behavior on the scale of a few hours. Simulations were found to be consistent with EISCAT radar and the ionosonde measurements (Marchaudon et al., 2018). For the long-term evolution of the plasmasphere-ionosphere system and during quiet conditions, IPIM simulations indicate that the plasmasphere is not stable in MLT and that no real dynamic equilibrium can be reached (Marchaudon and Blelly, 2020).

4.2 Plasmasphere models

Different plasmasphere models combining semi-empirical relations and physics-based backgrounds have been developed to reproduce the inner magnetosphere, the plasmopause, and even the plasma trough above the plasmasphere limit (see Pierrard et al., 2009 for a review of the plasmasphere models before 2009).

Pierrard and Stegen (2008) have developed the Belgian SWIFF Plasmasphere Model (BSPM), a 3D dynamic kinetic model of the plasmasphere. The BSPM model is based on physical mechanisms, including the interchange instability for the formation of the plasmopause (Pierrard and Lemaire, 2004), and provides the density and the temperature of the electrons, protons and other ions, both inside and outside the plasmasphere in the plasma trough. It has been coupled to the ionosphere (Pierrard and Voiculescu, 2011) using the IRI model as a boundary condition and is continuously improved by including other physical processes like

plasmopause thickness and plasmaspheric wind (Pierrard et al., 2021b). The input of the model is the date that determines the geomagnetic indices Kp and Dst. The plasmopause position does strongly correlate with the Bartels geomagnetic index, Kp index, which is retained as the main parameter used in the model to determine the plasmopause position. These indices may be predicted values when forecasting is required, or observed values when past events are simulated. They determine also the convection electric field. As BSPM uses the IRI model, it also depends on IRI parameters listed in Section 2. The BSPM model includes plasmopause erosion during geomagnetic storms as well as refilling, and is able to reproduce the plumes generated during storms and other structures like shoulders. It uses the kinetic approach that allows for the inclusion of non-Maxwellian distributions (Pierrard and Lemaire, 2001). The last version of the BSPM model is shown in Figures 1D–F for quiet, substorm, and storm activity. On 16 March 2015 1H (UT) with a quiet period with $K_p \sim 2$ (and almost constant during several hours), the plasmasphere is quite extended and almost circular (to compare with Figure 1A). A few hours later after a substorm injection on 16 March 2015 19 h (UT) with $K_p \sim 4$, there is formation of a plume in the dusk sector rotating with the Earth (to compare with Figure 1B). On 17 March 2015 21 h (UT) during an intense storm with $K_p = 8$, the model shows a strong erosion of the plasmasphere and formation of a long plume rotating with Earth (to relate with the statistics of Figure 1C).

The kinetic approach based on particle-in-cell simulations has also been combined with the fluid approach in Wang et al. (2015) to develop a dynamic fluid-kinetic model for plasma transport within the plasmasphere. A semi-kinetic model of plasmasphere refilling following geomagnetic storms has also been recently developed by Chatterjee and Schunk (2020b) and compared with hydrodynamic models to explore their differences. In hydrodynamic plasmasphere models, the non-linear inertial terms in the plasma transport equations are retained (Chatterjee, 2018; Chatterjee and Schunk, 2019; Chatterjee and Schunk, 2020a; Chatterjee and Schunk, 2020b). Limitations of such models are generally related to the difficulty to reproduce the mechanisms implicated in the formation of the plasmopause and the refilling process that is a key physics-based problem to solve to obtain a fully coupled plasmasphere-ionosphere model.

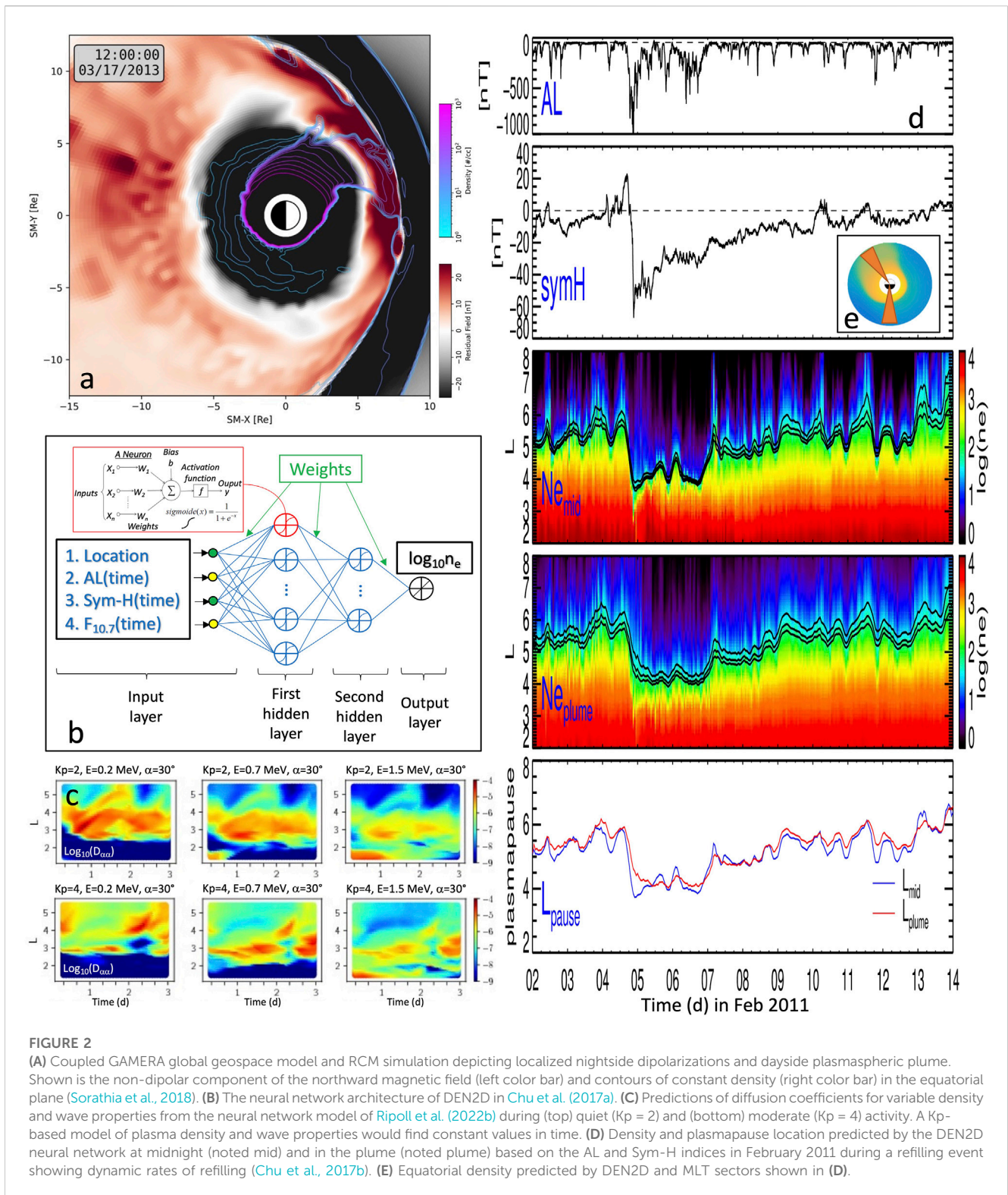
A two-dimensional physics-based plasmasphere model called Cold Plasma (CPL) (Jordanova et al., 2006; Jordanova et al., 2014) is used in a ring current-atmosphere interactions model of the source and loss processes of refilling and erosion driven by empirical inputs to simulate equatorial plasmaspheric electron densities. The performance of CPL has been evaluated against *in situ* measurements by the Van Allen Probes (Radiation Belt Storm Probes) for two events (De Pascuale et al., 2018). This study finds that severe erosion is best captured by an effective Kp-index for scaling the inner-magnetospheric potential governing E × B flows while refilling subsequent to moderate activity requires a solar wind parameterization of the quiet time background after the onset of a geomagnetic storm. Empirical models driving plasmasphere dynamics can be improved by capturing localized enhancements in electric field measurements and asymmetric profiles in electron density observations. More specific simulations were dedicated to comparisons with Van Allen Probes plasmopause observations (Goldstein et al., 2014a; Goldstein et al., 2016).

4.3 Plasmopause models

Physics-based models also provide the plasmopause location (e.g., Pierrard et al. (2021b)), with some models integrating Van Allen Probes measurements and plasma trough densities (e.g., Botek et al., 2021). Goldstein et al. (2003), Goldstein et al. (2005) developed a plasmopause test particle (PTP) dynamic model that represents the plasmaspheric boundary as an ensemble of E × B-drifting particles. The PTP model uses an electric field which is driven by the solar wind E field and Kp. The evolution of the plasmopause is modeled by the changing shape of the curve defined by the aggregate of the test particles evolving in a time-varying convection E-field. PTP simulation for the moderately disturbed interval 18–20 January 2000 shows a narrow drainage plume followed by significant plasmaspheric erosion, forming a second plume that coexists with the residue of the first plume (Goldstein et al., 2014b). Observations from three of the Los Alamos National Laboratory geostationary satellites are globally consistent with this PTP simulation in terms of the durations of plume sector transits while the MLT widths and timings of the simulated plumes do not precisely agree (Goldstein et al., 2014b). Goldstein et al. (2019) further generated a plasmopause statistical model from the simulations of 60 storms with $Dst_{PEAK} \leq -60nT$ based on Van Allen probes data yielding over 7 million model plasmopause locations. The epoch-binned PTP simulation results are combined in order to create an analytical plasmopause model for moderate storms ($-120nT \leq Dst_{PEAK} \leq -60nT$) and strong storms ($Dst_{PEAK} \leq -120nT$) that explicitly includes plumes. This model depends on the duskside plasmopause radius and two fitted coefficients, all three depend on epoch time (from -24 h to 36 h).

4.4 Global geospace model

A new promising approach is to couple a global geospace model of the magnetosphere with a physics-based density model. Figure 2 provides an example of the global geospace model, GAMERA (Zhang et al., 2017; Sorathia et al., 2020; Sorathia et al., 2021) coupled to RCM (Toffoletto et al., 2003). With a two-way coupling, these models are subparts of the Multiscale Atmosphere-Geospace Environment (MAGE) (e.g., Chen et al., 2021; Pham et al., 2021; Lin et al., 2022). The details of GAMERA's core MHD numerics and its verification are presented in Zhang et al. (2019). GAMERA uses high-order spatial reconstruction for the preservation of sharp structures. For typical MHD problems, Zhang et al. (2019) showed lower-order reconstruction (e.g., Second-order) requires four to eight times finer grid resolution (corresponding to a 250–4,000 factor increase of the cost resolution in 3D) as the higher-order (seventh- or eighth-order) reconstruction to reach the same accuracy. In addition to coupling the global MHD model to the inner magnetosphere model *via* ring current pressure ingestion (e.g., Pembroke et al., 2012), here the RCM is additionally evolving a cold fluid to model the evolution of the plasmaspheric density. In this coupling, the plasmasphere density is initialized using an empirical model (Gallagher et al., 2000) and refilling rate (Denton et al., 2012), and evolved using the same dynamically-calculated electrostatic potential as in the MHD simulation (e.g., Merkin and Lyon, 2010).



Note that RCM can further be coupled with SAMI3 as done by Huba et al. (2017b) to study the ionosphere-plasmasphere system response to the 17 March 2015 geomagnetic storm. The coupling occurs through the electrostatic potential equation (Huba et al., 2005; Huba and Sazykin, 2014) in which the conductance is defined by the sum of the conductance associated with solar

activity computed by SAMI3 and the auroral enhanced conductance provided by RCM.

Figure 2A depicts localized dipolarizations on the nightside and the formation of a dayside plasmaspheric plume during the 17 March 2013 geomagnetic storm (Sorathia et al., 2018). There is a complex interacting mesoscale process with nightside flows,

TABLE 3 First-principles physics models discussed in this article.

Name/References	Modeled quantity	Physics principles	Model validity domain	Known limitation
Ionosphere-Plasmasphere-Electrodynamics (IPE) (Maruyama et al., 2016)	3D densities for nine ion species, electron and ion temperatures, and parallel and perpendicular velocities of the ionosphere and plasmasphere	Parallel plasma transport based on the Field Line Interhemispheric Plasma (FLIP) Model Richards et al. (2010). Detailed model of the Earth's magnetic field using Apex coordinates Richmond (1995) and IGRF.	from 90 km to approximately 10,000 km	Lack of kinetic processes
IPIM Marchaudon and Blely (2015)	Ionosphere-plasmasphere model	2D interhemispheric fluid model for 6 ions coupled with a kinetic model for suprathermal electrons. Includes a chemistry solver	Defined for single L	Change of flux tube volume during a full rotation. Need an evolution of the chemistry in the D region
3DPM Pierrard and Stegen (2008)	Dynamic plasmopause, 3D Density	3D dynamic kinetic model	L = [2-8]	Sharp plasmopause
SPM (SWIFF Plasmaphere model) Pierrard and Voiculescu (2011)	Dynamic plasmopause, 3D Density	3D dynamic kinetic model, improved version by adding coupling with the ionosphere	from 60 km to L = 8	Limitations to reproduce the refilling process
BSPM (Belgian SWIFF Plasmasphere model) Pierrard et al. (2021b)	Dynamic plasmopause, 3D Density in plasmasphere and plasm trough	3D dynamic kinetic model coupled to the ionosphere, improved version by adding trough and refilling	from 60 km to L = 10	Plasmaspheric wind only on request
Wang et al. (2015)	Electron density along the magnetic field line	Dynamic fluid-kinetic model with an overlapped transition region (800 km–1,100 km in altitude)	Defined for single L	Limitations related to the difficulty to reproduce the mechanisms implicated in the formation of the plasmopause and the refilling process
Chatterjee and Schunk (2019), Chatterjee and Schunk (2020a)	1D hydrodynamic plasmasphere refilling model along magnetic flux tube	Fluid model. Three ions (H+, He+, and O+) and two neutrals (H and O)	Defined for single L	Discontinuities in the early to middle phases of refilling
Chatterjee and Schunk (2020b)	Density refilling: 1D spce and 1D velocity	Semi-kinetic model	Defined for single L	Do not include the effect of ion-neutral charge exchange mechanisms. 3D models needed for more detailed and thorough simulations
SAMI3 Huba and Krall (2013), Krall and Huba (2013)	3D Density, velocity, ion species	3D global ionosphere/plasmasphere fluid model. Use co-rotation potential, neutral wind dynamo potential, and a time-dependent Volland-Stern-Maynard-Chen potential. Use the partial donor cell method. 4-order flux-corrected transport scheme for E x B transport perpendicular to the magnetic field	Magnetic latitude range $\pm 88^\circ$. 90 km up to ~ 16 RE at the magnetic equator	Used in practice till L ~ 8 . Non-physical high-altitude 'top-down refilling' for single fluid
Cold Plasma (CPL) Jordanova et al. (2006), Jordanova et al. (2014)	Density with MLT dependence	2D fluid model	L in [1.75,6.6] (via continuity equation and prescribed empirical or self-consistent electric field)	Empirical refilling timescales determined from ionospheric measurements of Hedin (1987), and Bilitza (1986). Empirical saturated flux tube densities determined from ISEE observations of Carpenter and Anderson (1992)
RCM Toffoletto et al. (2003)	Density with MLT dependence	2D cold fluid to model the plasmaspheric density	L in [2,8]	No field-aligned density structure. Modeling plasmasphere refilling requires separate model, typically empirical refilling model like Denton et al. (2012)
Plasmopause test particle (PTP) dynamic model Goldstein et al. (2003), Goldstein et al. (2005)	Plasmopause with MLT dependence	Test-particle model	Validated at gobal scales (e.g., durations of plume sector transits)	Limited accuracy at meso-scales (e.g., MLT widths and timings of plumes)

(Continued on following page)

TABLE 3 (Continued) First-principles physics models discussed in this article.

Name/References	Modeled quantity	Physics principles	Model validity domain	Known limitation
Goldstein et al. (2019)	Plasmapause with MLT dependence	Statistical and analytical model based on PTP simulations	Dst < -60 nT	Defined for 2 types of storms: moderate ($-120\text{nT} \leq \text{Dst} \leq -60\text{nT}$) and strong ($\text{Dst} \leq -120\text{nT}$)

boundary Kelvin-Helmholtz on the dayside and flanks, and rolling dense plasmaspheric plume and structures. The plume is shown at 12 UT, i.e., 6 h after the CME impacted the Earth, with a typical expansion in the dusk-day sector that reaches L~6 and has started to roll around Earth.

The Kelvin-Helmholtz instability we see forming on the magnetopause and rolling side way of the magnetosphere (Merkin et al., 2013) may contribute to transfer shear and turbulence to the plume as it expands and removes pockets of dense plume plasma. In this way, the plume may potentially inherit a complex shape that is here captured by the global MHD model. The dense plasmasphere has a circular aspect for levels above 1,000 #/cc and there are structured plasma pockets of low density from 1-10 #/cc on the nightside beyond the main plasmapause gradient at L~3. On the night side, the magnetic field (and similarly the electric field) has a fine scale structure (with finger-like regions of higher field value) that reach the L~6 region and imprint a fluctuating profile to the dense pockets down to the plasmapause layer. As simulation resolution increases, some aspects of these structures become finer and more torturous. However, understanding the full cascade of energies down to the smallest scales requires global kinetic modeling.

These kinds of mesoscale structures play a critical role in shaping both the global-scale and micro-scale processes of the magnetosphere. Localized injections are believed to be an important part of the transport of magnetic flux and energetic particles into the inner magnetosphere (e.g., Gkioulidou et al., 2014; Merkin et al., 2019), thus building the large-scale ring current and affecting global dipolarization of the inner magnetosphere, as well as resulting in density enhancements at the dayside magnetopause that will alter local reconnection rates (e.g., Zhang et al., 2017) with potentially global consequences. Additionally, these mesoscale processes shape the different wave populations of the inner magnetosphere: anisotropic ion injections provide free energy for the ElectroMagnetic Ion Cyclotron (EMIC) wave population and the evolving plasmapause boundary correlates with the relative distribution of hiss and chorus waves, with important consequence on flux enhancements of energetic trapped particles in the radiation belts. Physics-based models discussed in this article are listed and succinctly synthesized in Table 3.

5 Machine learning models

Machine learning (ML) techniques have advanced significantly over the past decade, especially during the past few years, mainly due to three factors: enormously increased volumes of data, significantly improved algorithms, and substantially more-powerful computation hardware (especially Graphics Processing Unit (GPU) computation

that can accelerate the training by a factor of ~100) (Goodfellow et al., 2016). Although the applications of ML techniques are not entirely new in space physics, the unique combinations of the three aforementioned factors are leading to a new era where proper ML techniques could significantly enhance scientific progress, especially in understanding the non-linear nature of many physical processes. The combination of density data and models through machine learning techniques is one of the future and promising paths.

Taking advantage of the improvements in ML techniques and the extensive spatiotemporal coverage of NASA satellites, a series of ML-based models have been developed to study the cold plasma density for two purposes: 1) providing time- and history-dependent global distributions of total electron density in the Earth's magnetosphere, and 2) automatic detection of upper-hybrid-resonance frequency to calculate the total electron density.

A ML-based method was first proposed to reconstruct the global and time-varying distributions of any physical quantity Q that is sparsely sampled at various locations within the magnetosphere at any time (Bortnik et al., 2016). A feedforward neural network model was developed using point measurements of total electron density (i.e., cold plasma density) inferred from THEMIS spacecraft potential as an illustrative example. The model additionally takes the time series of the sym-H index as input and reconstructs global distributions of electron density at any time. Later, an optimized model of the electron density (DEN2D) near the equatorial plane was developed using THEMIS data (Chu et al., 2017a). The optimal input parameters of the DEN2D model are determined to be sym-H, AL, and F10.7 indices based on the neural network and neuron illustrated in Figure 2B. Time series of these indices are used as input so that the DEN2D model is both time- and history-dependent (i.e., dependent on a time sequence). The DEN2D model succeeds in reconstructing various plasmaspheric features during a geomagnetic storm, such as quiet time plasmasphere, erosion, and refilling of the plasmasphere and plume formation. Figures 2D, E shows the DEN2D density prediction extracted at both midnight and in the afternoon/day sector during plume expansion in February 2011. Analysis of these results demonstrated that refilling rates are dynamically changing (Chu et al., 2017b). The uncertainty of the DEN2D model can be estimated using a probabilistic model (Camporeale et al., 2019). Using global density profiles from the DEN2D model, it is shown that plasmaspheric hiss wave power is better parameterizing by plasma density rather than L shell, which should be adopted in current empirical models (Malaspina et al., 2018). A three-dimensional model of the electron density (DEN3D) was further developed using point measurements of the cold plasma density inferred from the upper hybrid resonance obtained from equatorial (ISEE and CRRES) and polar-orbiting satellites (POLAR and IMAGE). It has been verified using the additional measurements of density along the field line provided by IMAGE RPI (Chu et al., 2017b). The DEN2D and DEN3D models are shown

TABLE 4 Machine learning models of the electron density discussed in this article.

Name/References	Modeled quantity	Data in use (or type of physics)	Model validity domain	Known limitation
DEN2D Chu et al. (2017a)	Density with MLT dependence	THEMIS	L in [2, 8]	Same as DEN3D
DEN3D Chu et al. (2017b)	3D Density	ISEE, CRRES, POLAR, IMAGE	L in [1.5, 12]	Limited to the ranges of the training data, in spatial and activity coverage. Cannot usually make predictions during extreme geomagnetic storms
PINE Zhelavskaya et al. (2017)	Density with MLT dependence	Van Allen Probes	L in [1.75, 6.15]	Performance of neural networks limited by training data. No extreme geomagnetic storms in the PINE data
Neural network combined with physics-based model using Kalman filtering Zhelavskaya et al. (2021)	Density with MLT dependence	Neural network from Van Allen Probes (2012-2018) + Physics-based + Kalman filter	L in [1.75, 6.15]. Assimilation up to L = 10	Performance of neural networks limited by training data. No extreme geomagnetic storms in the PINE data. No MLT dependence of refilling rate. Too low density at low L-shell
Recurrent neural network model (encoder-decoder model) Huang et al. (2022)	Density with MLT dependence	Recurrent neural network model with encoder-decoder model with Long Short-Term Memory (LSTM) architecture. Van Allen Probes data	L in [1.75, 6.15]. Decoder of 270-min long. Encoder of 200-h long	Limited validation: model evaluated for only two plume events

to represent a large fraction of the observed variability in plasma density, with correlation coefficients on the order of 0.95, and a root-mean-square (rms) uncertainty about a factor of 2. There is room for improvement, since the model uncertainty is larger than the relative error of the underlying density measurements that are typically close to, or less than, 20% ([Reinisch et al., 2004](#)). For example, the confined density enhancements or depletions (ducts) may contribute to the model uncertainty since these localized structures may not be accurately predicted using geomagnetic indices. The DEN2D and DEN3D models can reconstruct the electron density with much smaller bias and error compared to previous empirical models (e.g., Global core plasma model ([Gallagher et al., 2000](#); [Sheeley et al., 2001](#); [Denton et al., 2004](#); [Denton et al., 2006](#)), and the model of [Ozhogin et al. \(2012\)](#)), although the model of [Ozhogin et al. \(2012\)](#) has competitive performance inside the plasmasphere at the lowest L shells. DEN3D's predictive ability provides unprecedented opportunities to gain insight into the 3-D behavior of plasmaspheric features (e.g., plasmaspheric erosion and refilling, as well as plume formation). Using a recurrent neural network, [Huang et al. \(2022\)](#) shows that the model could predict the formation and evolution of stable and evident plume configuration.

An electron density model of equatorial electron densities (PINE) was developed using Van Allen Probes measurements ([Zhelavskaya et al., 2017](#)). The PINE model also successfully reproduced erosion of the plasmasphere on the nightside and plume formation and evolution. However, ML-based models in space physics usually suffer from the problem of imbalanced dataset, i.e., many days of quiet conditions and a few days of storms ([Camporeale, 2019](#)). To overcome this difficulty, a coupled model was developed by using data assimilation, which is a weighted average of the neural-network-based PINE model for quiet times and a physics-based plasmaspheric model for active times, to provide the plasma density during both quiet times and geomagnetic storms ([Zhelavskaya et al., 2021](#)). In addition to

modeling electron density, a neural-network-based model was developed to reconstruct the time-varying plasmopause location near the equatorial plane, which outperformed previous empirical models within its database ([Guo et al., 2021](#)).

The application of ML density models in Fokker-Planck diffusion model has been performed in [Ma et al. \(2018\)](#) and [Bortnik et al. \(2018\)](#). Neural networks (and other ML techniques) can also be used to perform assimilation and interpolation/extrapolation of large datasets. Diffusion coefficients computed from variable density and wave properties are directly embedded in a machine learning model in [Kluth et al. \(2022\)](#). Predictions of this model for 3 days of quiet ($K_p = 2$) and moderate ($K_p = 4$) times following the storm are shown in [Figure 2C](#) ([Ripoll et al., 2022b](#)). Temporal variations are related to the simultaneous change of density and wave properties, calling for future models that will couple density and wave properties together. A K_p -based model of density and wave properties, as commonly used nowadays, would find constant values of the diffusion coefficients in time at fixed L-shell in [Figure 2C](#) while the ML model shows multiple variations with time.

The ML techniques can also be applied to labor-intensive tasks. For example, the electron densities can be inferred from plasma wave spectra, which can be both time-consuming and challenging (e.g., [Kurth et al., 2015](#)). A neural-network-based upper hybrid resonance (UHR) determination algorithm (NURD) was developed to automatically determine the electron density from plasma wave measurements using Van Allen Probes data ([Zhelavskaya et al., 2016, 2018; 2020](#)). NURD is applied to Van Allen Probes EMFISIS data in [Allison et al. \(2021\)](#) to show that the plasma density has a controlling effect over acceleration of radiation belt electrons to ultra-relativistic energies. ML-based methods for automatically determining the UHR frequency have also been applied to the Arase satellite using convolutional neural network ([Hasegawa et al., 2019; Matsuda et al., 2020](#)) and the CLUSTER mission using several automated pipelines based on neural network

methods (Gilet et al., 2021). Machine models of the electron density discussed in this article are listed and succinctly synthesized in Table 4.

6 Conclusion and perspectives

This review article strictly focuses on existing plasma density models, with an emphasis on those most commonly used (or most recent or promising) in radiation belt physics or space weather codes. Plasma density models describe the state of the plasmasphere in radiation belt simulations and are at the heart of the coupling between the ionosphere, which provides the plasma source, and the magnetosphere, wherein the intensity and variability of wave-particle interactions are conditioned by the plasma density (see Thaller et al., 2022 and references therein). All models discussed in this review article are listed in Tables 1, 2, 3, 4 with their main properties listed.

This review shows that most of the current empirical density or plasmopause models in use for the last decade are relatively simple in their geomagnetic activity dependence, often including a dependence on a single geomagnetic index, e.g., Kp (Carpenter and Anderson (1992)), and not including a magnetic local time dependence. Some of these models are incomplete, limited by either short temporal coverage, such as those extracted from CRRES measurements (e.g., O'Brien and Moldwin, 2003), or omitting magnetic local time sectors (Carpenter and Anderson (1992)) or geomagnetic activity (Ozhogin et al. (2012)). The variability of the electron plasma density is also very large when sorted with a single index, even if retaining magnetic local time dependence (see Figure 3 of Ripoll et al., 2022a). The spatial and temporal variations in plasma density depend on multiple parameters, such as the refilling rate, which is itself dependent on UV irradiance, the state of the thermosphere (neutral winds, composition, etc.), and the time history and level of convective processes due to geomagnetic activity, the coupling between the magnetosphere and ionosphere, particle precipitation, and other processes. For instance, the standard deviation of the 100 #/cc density level (assimilable to the plasmopause) varies from $\sim\pm 0.5L$ for quiet times ($Kp < 2$, $AE < 300$, $Dst > -50$) up to $\sim\pm 1L$ for active times (Ripoll et al., 2022a). This variability can be explained from the multiple factors that influence the plasmaspheric density. For instance, Denton et al. (2006) retained in their plasma mass density model, the F10.7 EUV index, magnetic local time, the solar wind dynamic pressure P_{dyn} , the phase of the year, and the solar wind B_z in GSM coordinates (parameters listed in order of decreasing importance). Chu et al. (2017a) found the optimal input parameters of the neural network DEN2D model are the sym-H, AL, and F10.7 indices. This highlights that new models should keep the main parameter dependences, including ionospheric and geomagnetic variability, and the MLT dependence.

Density variations are well observed between $L\sim 1.5$ and $L\sim 6$ at each pass of the Van Allen Probes (see Figure 2F in Ripoll et al., 2017), thus directly influencing the diffusion coefficients describing wave particle interactions in the radiation belts. Diffusion coefficients vary linearly with the electron plasma frequency, $f_{pe}(N)$, however changes in density further correlate with changes in the power of plasmaspheric hiss waves, which typically reside

within the plasmasphere. Wave power is found to increase as density increases (Malaspina et al., 2016; Malaspina et al., 2018; Thomas et al., 2021). As a result, the simultaneous change in both density and hiss power leads to strong and complex variations of the diffusion coefficients (see Figure 5 in Ripoll et al., 2017). For instance, substorm activity causes short duration (within ± 4 h) reductions in density, and therefore a lowering of the amplitude of the whistler-mode waves within the plasmasphere. Variation in these parameters causes opposite effects in terms of pitch angle diffusion and, eventually, an overall decrease of pitch-angle diffusion during the main substorm activity (Ripoll et al., 2020b). Therefore, an accurate description of the plasma density, and its variation with geomagnetic activity, directly impacts the accuracy of modeling wave particle interactions.

The large number of parameters and mutually interdependent processes operating over different spatial and temporal scales, as just described, require models that include detailed physics or use machine learning methods in order to accurately capture or model these diverse plasma density features. Physics-based models have progressed well in the last decade, for instance, from 2D to 3D (e.g., Huba and Krall, 2013; Pierrard et al., 2021b) or by introducing new physical models or couplings, for instance, with detailed atmospheric sources (e.g., Huba and Liu, 2020). Physics-based models intrinsically simulate the geomagnetic activity and can retain various geomagnetic indices, whether these codes are limited to the atmosphere/ionosphere/plasmasphere system or are more global MHD codes, such as the MAGE-GAMERA project (e.g., Sorathia et al., 2021). It is only nowadays that physics-based models have started to be coupled with radiation belt codes (e.g., Dahmen et al., 2022), due to the overall complexity and multiplicity of the physical processes modeled in radiation belt codes (Ripoll et al., 2020a). An undeniable strength of physics-based models is that they can mitigate the inherent limitations of sparse spatial coverage of the data, in particular for active times (e.g., Zhelavskaya et al., 2021). Machine learning models also account intrinsically for multiple dependences (e.g., Chu et al., 2017a; Zhelavskaya et al., 2021), and are undoubtedly a promising approach to combine multiple satellite observations and produce the next-generation of global empirical plasma density models. A neural network-based density model has recently served to show that the plasma density has a controlling effect over acceleration of radiation belt electrons to ultra-relativistic energies (Allison et al., 2021). Contrary to empirical fits that do not allow trustable extrapolation, machine learning techniques, such as neural networks, are extremely promising in terms of predictive capability, which is a keystone for space weather codes. Progress in neural network techniques are also expected in the coming years. For instance, the use of the recent physics-informed neural networks (e.g., Raissi et al., 2019), in which the neural network is constrained to respect any given physical law described by general non-linear partial differential equations, could be an hybrid way between physics-based models and machine learning techniques, possibly well applying to plasma density modeling. Finally, the close relationship between plasmaspheric waves and plasmaspheric density also highlights the need for more coupling between them, whether that coupling is done when generating physical

models or embedded within macroscopic quantities such as diffusion coefficients (e.g., Kluth et al., 2022).

In any case, all models eventually aim to capture the effect caused by magnetic local time variations of the plasma density for various geomagnetic conditions. There is an undeniable need of new measurements to support model development and validation. However, most measurements of the electron density used to build and/or validate these models, are often single observation per time at a single location in space, leading to a reliance on statistics to capture the magnetic local time resolution. This reliance on statistics means that the dynamics at any given location are averaged over, resulting in the loss of some of the structures, their rate of change, and motion at any given spatial location. This limitation is difficult to overcome, even when combining observations from multiple satellites with machine learning techniques. Future missions should consider the use of multiple spacecraft/cubesats azimuthally separated across various magnetic local times in order to provide better coverage and resolution of plasma density dynamics coupled with simultaneous measurements of the ambient electromagnetic waves, which ultimately impact the models used in radiation belt and space weather codes.

Author contributions

J-FR conceptualized and led the study. J-FR wrote the manuscript with the contribution of VP (Section 4), GC (Section 2 and Section 3), XC (Section 5), KS, and VM (Section 4). J-FR created Tables 1, 2, 3, 4. ST treated the Van Allen Probes B EFW data presented in Figures 1A–C. VP ran the SPM code to generate Figures 1D–F. DH performed model computation in Figures 1G, H. KS performed Gamera runs to generate Figure 2A. J-FR generated Figures 2B, C. XC generated Figures 2D, E. All authors contributed to writing of the manuscript through reviews and edits.

Funding

NSF-GEM grant 2040708. NASA grant 80NSSC20K1324. Horizon 2020 PITHIA-NRF grant agreement No. 101007599. EURAMET's European Partnership on Metrology project 21GRD02 BIOSPHERE. US DOE DE-AC05-00OR22725. LANL project 20220453ER, ANR ASTRID project "PACTE-ESPACE".

References

- Albert, J. M. (1999). Analysis of quasi-linear diffusion coefficients. *J. Geophys. Res.* 104, 2429–2441. doi:10.1029/1998JA900113
- Allison, H. J., Shprits, Y. Y., Zhelavskaya, I. S., Wang, D., and Smirnov, A. G. (2021). Gyroresonant wave-particle interactions with chorus waves during extreme depletions of plasma density in the Van Allen radiation belts. *Sci. Adv.* 7, eabc0380. doi:10.1126/sciadv.abc0380
- Angerami, J. J., and Thomas, J. O. (1964). Studies of planetary atmospheres: 1. The distribution of electrons and ions in the earth's exosphere. *J. Geophys. Res.* 69 (21), 4537–4560. doi:10.1029/JZ069i021p04537
- Bandić, M., Verbanac, G., Moldwin, M. B., Pierrard, V., and Piredda, G. (2016). MLT dependence in the relationship between plasmopause, solar wind, and geomagnetic activity based on CRRES: 1990–1991. *J. Geophys. Res. Space Phys.* 121, 4397–4408. doi:10.1002/2015JA022278
- Bandic, M., Verbanac, G., Pierrard, V., and Cho, J. (2017). Evidence of MLT propagation of the plasmopause inferred from THEMIS data. *J. Atmosph. Sol.-Terr. Phys.* 161, 55–63. doi:10.1016/j.jastp.2017.05.005
- Berube, D., Moldwin, M. B., Fung, S. F., and Green, J. L. (2005). A plasmaspheric mass density model and constraints on its heavy ion concentration. *J. Geophys. Res.* 110, A04212. doi:10.1029/2004JA010684
- Bilitza, D., and Reinisch, B. W. (2008). International reference ionosphere 2007: Improvements and new parameters. *Adv. Space Res.* 42 (4), 599–609. doi:10.1016/j.asr.2007.07.048
- Bilitza, D., Altadill, D., Truhlik, V., Shubin, V., Galkin, I., Reinisch, B., et al. (2017). International Reference Ionosphere 2016: From ionospheric climate to real-time weather predictions. *Space weather.* 15, 418–429. doi:10.1002/2016sw001593
- Bilitza, D., Altadill, D., Zhang, Y., Mertens, C., Truhlik, V., Richards, P., et al. (2014). The international reference ionosphere 2012 – A model of international collaboration. *J. Space Weather Space Clim.* 4, A07–A12. doi:10.1051/swsc/2014004
- Bilitza, D. (1986). International reference ionosphere: Recent developments. *Radio Sci.* 21 (3), 343–346. doi:10.1029/RS021i003p0343
- Bilitza, D. (2018). IRI the international standard for the ionosphere. *Adv. Radio Sci.* 16, 1–11. doi:10.5194/ars-16-1-2018

Acknowledgments

The authors thank the EFW and EMFISIS teams of the Van Allen Probes mission for their support. This research was supported by the International Space Science Institute (ISSI) in Bern, through ISSI International Team project #477 (Radiation Belt Physics From Top To Bottom: Combining Multipoint Satellite Observations And Data Assimilative Models To Determine The Interplay Between Sources And Losses). The work of J-FR and GC was performed under the auspices of an agreement between CEA/DAM (Commissariat à l'Énergie Atomique, Direction des Applications Militaires) and NNSA/DP (National Nuclear Security Administration, Defense Program) on cooperation on fundamental science. J-FR thank the Direction Générale de l'Armement (DGA) and the Agence pour l'Innovation de Défense (AID) for funding the ASTRID project "PACTE-ESPACE". DH, GC, and J-FR acknowledge NSF-GEM grant 2040708. DH acknowledges NASA grant 80NSSC20K1324. VP acknowledges the Horizon 2020 PITHIA-NRF grant agreement No. 101007599 and the EURAMET's European Partnership on Metrology project 21GRD02 BIOSPHERE. SD acknowledges support by the US DOE under contracts DE-AC05-00OR22725. GD was supported by the Laboratory Directed Research and Development program at Los Alamos National Laboratory (LANL) under project 20220453ER.

Conflict of interest

ST was employed by the company Orion Space Solutions.

The remaining authors declare that the research was conducted in the absence of any commercial or financial relationships that could be construed as a potential conflict of interest.

Publisher's note

All claims expressed in this article are solely those of the authors and do not necessarily represent those of their affiliated organizations, or those of the publisher, the editors and the reviewers. Any product that may be evaluated in this article, or claim that may be made by its manufacturer, is not guaranteed or endorsed by the publisher.

- Bortnik, J., Chu, X., Ma, Q., Li, W., Zhang, X., Thorne, R. M., et al. (2018). "Artificial neural networks for determining magnetospheric conditions," in *Machine learning techniques for space weather*. Editors E. Camporeale, S. Wing, and J. R. Johnson (Netherlands: Elsevier), 279–300. doi:10.1016/b978-0-12-811788-0.00011-1
- Bortnik, J., Li, W., Thorne, R. M., and Angelopoulos, V. (2016). A unified approach to inner magnetospheric state prediction. *J. Geophys. Res. Space Phys.* 121 (3), 2423–2430. doi:10.1002/2015ja021733
- Botek, E., Pierrard, V., and Darrouzet, F. (2021). Assessment of the Earth's cold plasmatrrough modeling by using Van Allen Probes/EMFISIS and Arase/PWE electron density data. *J. Geophys. Res. Space Phys.* 126. doi:10.1029/2021JA029737
- Camporeale, E., Chu, X., Agapitov, O. V., and Bortnik, J. (2019). On the generation of probabilistic forecasts from deterministic models. *Space weather*. 17, 455–475. doi:10.1029/2018SW002026
- Camporeale, E. (2019). The challenge of machine learning in Space Weather: Nowcasting and forecasting. *Space weather*. 17, 1166–1207. doi:10.1029/2018SW002061
- Carpenter, D. L., and Anderson, R. R. (1992). An ISEE/whistler model of equatorial electron density 740 in the magnetosphere. *J. Geophys. Res.* 97 (A2), 1097–1108. doi:10.1029/91JA01548
- Carpenter, D. L., Anderson, R. R., Calvert, W., and Moldwin, M. B. (2000). CRRES observations of density cavities inside the plasmasphere. *J. Geophys. Res.* 105 (10), 23323–23338. doi:10.1029/2000JA000013
- Carpenter, D. L., and Smith, R. L. (1964). Whistler measurements of electron density in the 738 magnetosphere. *Rev. Geophys. Space Phys.* 2, 415. doi:10.1029/91JA01548
- Carpenter, D. L. (1963). Whistler evidence of a 'knee' in the magnetospheric ionization density profile. *J. Geophys. Res.* 68, 1675–1682. doi:10.1029/jz068i006p01675
- Carpenter, D. L. (1966). Whistler studies of the plasmopause in the magnetosphere, I, Temporal variations in the position of the knee and some evidence on plasma motions near the knee. *J. Geophys. Res.* 71, 693–709. doi:10.1029/jz071i003p00693
- Cervantes, S., Shprits, Y. Y., Aseev, N. A., and Allison, H. J. (2020a). Quantifying the effects of EMIC wave scattering and magnetopause shadowing in the outer electron radiation belt by means of data assimilation. *J. Geophys. Res. Space Phys.* 125, e2020JA028208. doi:10.1029/2020JA028208
- Cervantes, S., Shprits, Y. Y., Aseev, N. A., Drozdov, A. Y., Castillo, A., and Stolle, C. (2020b). Identifying radiation belt electron source and loss processes by assimilating spacecraft data in a three-dimensional diffusion model. *J. Geophys. Res. Space Phys.* 125, e2019JA027514. doi:10.1029/2019JA027514
- Chatterjee, K., and Schunk, R. W. (2019). A multiion, flux-corrected transport based hydrodynamic model for the plasmasphere refilling problem. *J. Geophys. Res. Space Phys.* 125 (1), 250. doi:10.1029/2019JA026834
- Chatterjee, K., and Schunk, R. W. (2020b). A semikinetic model of plasmasphere refilling following geomagnetic storms and comparison with hydrodynamic results. *J. Geophys. Res. Space Phys.* 125, e2020JA028016. doi:10.1029/2020JA028016
- Chatterjee, K., and Schunk, R. W. (2020a). The development and validation of a "flux-corrected transport" based solution methodology for the plasmasphere refilling problem following geomagnetic storms. *Earth, Planets Space* 72 (26), 26. doi:10.1186/s40623-020-01150-0
- Chatterjee, K. (2018). The development of hydrodynamic and kinetic models for the Plasmasphere refilling problem following a geomagnetic storm. Available at: <https://digitalcommons.usu.edu/etd/7364>.
- Chen, X., Dang, T., Zhang, B., Lotko, W., Pham, K., Wang, W., et al. (2021). Global effects of a polar solar eclipse on the coupled magnetosphere-ionosphere system. *Geophys. Res. Lett.* 48, e2021GL096471. doi:10.1029/2021GL096471
- Cho, J., Lee, D.-Y., Kim, J.-H., Shin, D.-K., Kim, K.-C., and Turner, D. (2015). New model fit functions of the plasmopause location determined using THEMIS observations during the ascending phase of solar cycle 24. *J. Geophys. Res. Space Phys.* 120, 2877–2889. doi:10.1002/2015JA021030
- Chu, X., Bortnik, J., Li, W., Ma, Q., Angelopoulos, V., and Thorne, R. M. (2017b). Erosion and refilling of the plasmasphere during a geomagnetic storm modeled by a neural network. *J. Geophys. Res. Space Phys.* 122 (7), 7118–7129. doi:10.1002/2017ja023948
- Chu, X., Bortnik, J., Li, W., Ma, Q., Denton, R., Yue, C., et al. (2017a). A neural network model of three-dimensional dynamic electron density in the inner magnetosphere. *J. Geophys. Res. Space Phys.* 122 (9), 9183–9197. doi:10.1002/2017ja024464
- Coisson, P., Radicella, S. M., Leitinger, R., and Nava, B. (2006). Topside electron density in IRI and NeQuick: Features and limitations. *Adv. Space Res.* 37 (5), 937–942. doi:10.1016/j.asr.2005.09.015
- Dahmen, N., Sicard, A., Brunet, A., Santolik, O., Pierrard, V., Botek, E., et al. (2022). Farwest: Efficient computation of wave-particle interactions for a dynamic description of the electron radiation belt diffusion. *J. Geophys. Res. Space Phys.* 127, e2022JA030518. doi:10.1029/2022JA030518
- Darrouzet, F., and De Keyser, J. (2013). The dynamics of the plasmasphere: Recent results. *J. Atmos. Solar-Terrestrial Phys.* 99, 53–60. doi:10.1016/j.jastp.2012.07.004
- De Pascuale, S., Jordanova, V. K., Goldstein, J., Kletzing, C. A., Kurth, W. S., Thaller, S. A., et al. (2018). Simulations of Van Allen Probes plasmaspheric electron density observations. *J. Geophys. Res. Space Phys.* 123, 9453–9475. doi:10.1029/2018JA025776
- Delzanno, G. L., Borovsky, J. E., Henderson, M. G., Resendiz Lira, P. A., Roytershteyn, V., and Welling, D. T. (2021). The impact of cold electrons and cold ions in magnetospheric physics. *J. Atmos. Solar-Terrestrial Phys.* 220, 105599. doi:10.1016/j.jastp.2021.105599
- Denton, R. E., Menietti, J. D., Goldstein, J., Young, S. L., and Anderson, R. R. (2004). Electron density in the magnetosphere. *J. Geophys. Res.* 109, A09215. doi:10.1029/2003JA010245
- Denton, R. E., Takahashi, K., Galkin, I. A., Nsumei, P. A., Huang, X., Reinisch, B. W., et al. (2006). Distribution of density along magnetospheric field lines. *J. Geophys. Res.* 111, A04213. doi:10.1029/2005JA011414
- Denton, R. E., Wang, Y., Webb, P. A., Tengdin, P. M., Goldstein, J., Redfern, J. A., et al. (2012). Magnetospheric electron density long-term (>1 day) refilling rates inferred from passive radio emissions measured by IMAGE RPI during geomagnetically quiet times. *J. Geophys. Res. Space Phys.* 117. doi:10.1029/2011ja017274
- Escoubet, J., Song, P., Reinisch, B. W., and Green, J. L. (2007). Smooth electron density transition from plasmasphere to the subauroral region. *J. Geophys. Res.* 112, A05227. doi:10.1029/2007JA012298
- Fuller-Rowell, T. J., Akmaev, R. A., Wu, F., Anghel, A., Maruyama, N., Anderson, D. N., et al. (2008). Impact of terrestrial weather on the upper atmosphere. *Geophys. Res. Lett.* 35, L09808. doi:10.1029/2007GL032911
- Gallagher, D. L., Craven, P. D., and Comfort, R. H. (2000). Global core plasma model. *J. Geophys. Res. Space Phys.* 105, 18819–18833. doi:10.1029/1999JA000241
- Gilet, N., De Leon, E., Gallé, R., Vallières, X., Rauch, J.-L., Jegou, K., et al. (2021). Automatic detection of the thermal electron density from the WHISPER experiment onboard CLUSTER-II mission with neural networks. *J. Geophys. Res. Space Phys.* 126, e2020JA028901. doi:10.1029/2020JA028901
- Gkioulidou, M., Ukhorskiy, A. Y., Mitchell, D. G., Sotirelis, T., Mauk, B. H., and Lanzerotti, L. J. (2014). The role of small-scale ion injections in the buildup of Earth's ring current pressure: Van Allen Probes observations of the 17 March 2013 storm. *J. Geophys. Res. Space Phys.* 119, 7327–7342. doi:10.1002/2014ja020096
- Glauert, S. A., and Horne, R. B. (2005). Calculation of pitch angle and energy diffusion coefficients with the PADIE code. *J. Geophys. Res.* 110, A04206. doi:10.1029/2004JA010851
- Goldstein, J., Baker, D. N., Blake, J. B., De Pascuale, S., Funsten, H. O., Jaynes, A. N., et al. (2016). The relationship between the plasmapause and outer belt electrons. *J. Geophys. Res. Space Phys.* 121, 8392–8416. doi:10.1002/2016JA023046
- Goldstein, J., Burch, J. L., and Sandel, B. R. (2005). Magnetospheric model of subauroral polarization stream. *J. Geophys. Res.* 110, A09222. doi:10.1029/2005JA011135
- Goldstein, J., De Pascuale, S., Kletzing, C., Kurth, W., Genestreti, K. J., Skoug, R. M., et al. (2014a). Simulation of van allen probes plasmapause encounters. *J. Geophys. Res. Space Phys.* 119, 7464–7484. doi:10.1002/2014JA020252
- Goldstein, J., Pascuale, S., and Kurth, W. S. (2019). Epoch-based model for stormtime plasmapause location. *J. Geophys. Res.* 124, 4462–4491. doi:10.1029/2018JA025996
- Goldstein, J. (2006). Plasmasphere response: Tutorial and review of recent imaging results. *Space Sci. Rev.* 124, 203–216. doi:10.1007/s11214-006-9105-y
- Goldstein, J., Sandel, B. R., Hairston, M. R., and Reiff, P. H. (2003). Control of plasmaspheric dynamics by both convection and sub-auroral polarization stream. *Geophys. Res. Lett.* 30 (24), 2243. doi:10.1029/2003GL018390
- Goldstein, J., Thomsen, M. F., and DeJong, A. (2014b). *In situ* signatures of residual plasmaspheric plumes: Observations and simulation. *J. Geophys. Res. Space Phys.* 119, 4706–4722. doi:10.1002/2014JA019953
- Goodfellow, I., Bengio, Y., Courville, A., and Bengio, Y. (2016). *Deep learning*. Cambridge: MIT press.
- Gulyaeva, T. L., Arikani, F., and Stanislawski, I. (2011). Inter-hemispheric imaging of the ionosphere with the upgraded IRI-Plas model during the space weather storms. *Earth Planet Sp.* 63, 929–939. doi:10.5047/eps.2011.04.007
- Gulyaeva, T. L. (2012). Empirical model of ionospheric storm effects on the F2 layer peak height associated with changes of peak electron density. *J. Geophys. Res.* 117, A02302. doi:10.1029/2011JA017158
- Gulyaeva, T. L., Huang, X., and Reinisch, B. W. (2002). Plasmaspheric extension of topside electron density profiles. *Adv. Space Res.* 29 (6), 825–831. doi:10.1016/s0273-1177(02)00038-8
- Gulyaeva, T. L. (2011). Storm time behavior of topside scale height inferred from the ionosphere-plasmasphere model driven by the F2 layer peak and GPS-TEC observations. *Adv. Space Res.* 47, 913–920. doi:10.1016/j.asr.2010.10.025
- Guo, D., Fu, S., Xiang, Z., Ni, B., Guo, Y., Feng, M., et al. (2021). Prediction of dynamic plasmapause location using a neural network. *Space weather*. 19, e2020SW002622. doi:10.1029/2020SW002622
- Hain, K. (1987). The partial donor cell method. *J. Comput. Phys.* 73, 131–147. doi:10.1016/0021-9991(87)90110-0
- Hartley, D. P., Cunningham, G. S., Ripoll, J.-F., Malaspina, D. M., Kasahara, Y., Miyoshi, Y., et al. (2023). *Using van allen probes and Arase observations to develop an empirical plasma density model in the inner zone*. *J. Geophys. Res. Space Phys.*, in press.
- Hartley, D. P., Kletzing, C. A., Kurth, W. S., Bounds, S. R., Averkamp, T. F., Hospodarsky, G. B., et al. (2016). Using the cold plasma dispersion relation and whistler mode waves to

- quantify the antenna sheath impedance of the Van Allen Probes EFW instrument. *J. Geophys. Res. Space Physics* 121, 4590–4606. doi:10.1002/2016JA022501
- Hasegawa, T., Matsuda, S., Kumamoto, A., Tsuchiya, F., Kasahara, Y., Miyoshi, Y., et al. (2019). Automatic electron density determination by using a convolutional neural network. *IEEE Access* 7, 163384–163394. doi:10.1109/ACCESS.2019.2951916
- He, F., Zhang, X.-X., Lin, R.-L., Fok, M.-C., Katus, R. M., Liemohn, M. W., et al. (2017). A new solar wind-driven global dynamic plasmapause model: 2. Model and validation. *J. Geophys. Res. Space Physics* 122, 7172–7187. doi:10.1002/2017JA023913
- Hedin, A. E. (1987). MSIS-86 thermospheric model. *J. Geophys. Res.* 92 (A5), 4649–4662. doi:10.1029/JA092iA05p04649
- Helmboldt, J. F., and Hurley-Walker, N. (2020). Ionospheric irregularities observed during the GLEAM survey. *Radio Sci.* 55, e2020RS007106. doi:10.1029/2020RS007106
- Huang, S., Li, W., Shen, X.-C., Ma, Q., Chu, X., Ma, D., et al. (2022). Application of recurrent neural network to modeling Earth's global electron density. *J. Geophys. Res. Space Phys.* 127, e2022JA030695. doi:10.1029/2022JA030695
- Huang, X., Reinisch, B. W., Song, P., Green, J. L., and Gallagher, D. L. (2004). Developing an empirical density model of the plasmasphere using IMAGE/RPI observations. *Adv. Space Res.* 33, 829–832. doi:10.1016/j.asr.2003.07.007
- Huba, J. D. (2023). Resolution of the equatorial spread F problem: Revisited. *Front. Astron. Space Sci.* 9, 1098083. doi:10.3389/fspas.2022.1098083
- Huba, J. D. (2003). "A tutorial on Hall magnetohydrodynamics," in *Space simulations*. Editors M. Scholer, C. T. Dum, and J. Büchner (New York: Springer), 170.
- Huba, J. D., Joyce, G., and Fedder, J. A. (2000). Sami2 (Sami2 is another model of the ionosphere): A new low-latitude ionosphere model. *J. Geophys. Res.* 105 (10), 53.
- Huba, J. D., Joyce, G., Sazykin, S., Wolf, R., and Spiro, R. (2005). Simulation study of penetration electric field effects on the low-to mid-latitude ionosphere. *Geophys. Res. Lett.* 32, L23101. doi:10.1029/2005GL024162
- Huba, J. D., and Krall, J. (2013). Modeling the plasmasphere with Sami3. *Geophys. Res. Lett.* 40, 6–10. doi:10.1029/2012GL054300
- Huba, J. D., and Liu, H.-L. (2020). Global modeling of equatorial spread F with Sami3/WACCM-X. *Geophys. Res. Lett.* 47, e2020GL088258. doi:10.1029/2020GL088258
- Huba, J. D., Maute, A., and Crowley, G. (2017). Sami3_ICON: Model of the ionosphere/plasmasphere system. *Space Sci. Rev.* 212, 731–742. doi:10.1007/s11214-017-0415-z
- Huba, J. D., Sazykin, S., and Coster, A. (2017b). Sami3-RCM simulation of the 17 March 2015 geomagnetic storm. *J. Geophys. Res. Space Phys.* 122, 1246–1257. doi:10.1002/2016JA023341
- Huba, J. D., and Sazykin, S. (2014). Storm time ionosphere and plasmasphere structuring: Sami3-RCM simulation of the 31 March 2001 geomagnetic storm. *Geophys. Res. Lett.* 41, 8208–8214. doi:10.1002/2014GL062110
- Hysell, D. L., Fang, T. W., and Fuller-Rowell, T. J. (2022). Modeling equatorial F-region ionospheric instability using a regional ionospheric irregularity model and WAM-IPE. *J. Geophys. Res. Space Phys.* 127, e2022JA030513. doi:10.1029/2022JA030513
- Jacobson, A. R., and Erickson, W. C. (1993). Observations of electron density irregularities in the plasmasphere using the VLA radio interferometer. *Ann. Geophys.* 11 (10), 869–888.
- Jahn, J., Goldstein, J., Kurth, W., Thaller, S., De Pascuale, S., Wygant, J., et al. (2020). Determining plasmaspheric density from the upper hybrid resonance and from spacecraft potential: How do they compare? *J. Geophys. Res. Space Phys.* 125, 1–17.
- Jordanova, V. K., Miyoshi, Y. S., Zaharia, S., Thomsen, M. F., Reeves, G. D., Evans, D. S., et al. (2006). Kinetic simulations of ring current evolution during the geospace environment modeling challenge events. *J. Geophys. Res.* 111, A11S10. doi:10.1029/2006JA011644
- Jordanova, V. K., Yu, Y., Niehof, J. T., Skoug, R. M., Reeves, G. D., Kletzing, C. A., et al. (2014). Simulations of inner magnetosphere dynamics with an expanded RAM-SCB model and comparisons with Van Allen Probes observations. *Geophys. Res. Lett.* 41, 2687–2694. doi:10.1002/2014GL059533
- Kim, K. C., Shprits, Y., Subbotin, D., and Ni, B. (2011). Understanding the dynamic evolution of the relativistic electron slot region including radial and pitch angle diffusion. *J. Geophys. Res.* 116, A10214. doi:10.1029/2011JA016684
- Kletzing, C. A., Kurth, W. S., Acuna, M., MacDowall, R. J., Torbert, R. B., Averkamp, T., et al. (2013). The electric and magnetic field instrument suite and integrated science (EMFISIS) on RBSP. *Space Sci. Rev.* 179, 127–181. doi:10.1007/s11214-013-9993-6
- Kluth, G., Ripoll, J.-F., Has, S., Fischer, A., and Mougeot, M. (2022). Machine learning methods applied to the global modeling of event-driven pitch angle diffusion coefficients during high-speed streams. *Front. Phys.* 10, 786639. doi:10.3389/fphy.2022.786639
- Kotova, G. A. (2007). The Earth's plasmasphere: State of studies (a review). *Geomagnetism Aeronomy* 47 (4), 409–422. doi:10.1134/s0016793207040019
- Krall, J., and Huba, J. D. (2021). Counterstreaming cold H⁺, He⁺, O⁺, and N⁺ outflows in the plasmasphere. *Front. Astron. Space Sci.* 8, 712611. doi:10.3389/fspas.2021.712611
- Krall, J., Huba, J. D., and Borovsky, J. E. (2018). Sami3 simulations of a persistent plasmasphere plume. *Geophys. Res. Lett.* 45, 3374–3381. doi:10.1002/2017GL076448
- Krall, J., and Huba, J. D. (2013). Sami3 simulation of plasmasphere refilling. *Geophys. Res. Lett.* 40, 2484–2488. doi:10.1002/grl.50458
- Krall, J., and Huba, J. (2019). Simulation of counterstreaming H⁺ outflows during plasmasphere refilling. *Geophys. Res. Lett.* 46, 3052–3060. doi:10.1029/2019GL082130
- Kurth, W. S., De Pascuale, S., Faden, J. B., Kletzing, C. A., Hospodarsky, G. B., Thaller, S., et al. (2015). Electron densities inferred from plasma wave spectra obtained by the Waves instrument on Van Allen Probes. *J. Geophys. Res. Space Phys.* 120, 904–914. doi:10.1002/2014JA020857
- Kwon, H.-J., Kim, K.-H., Jee, G., Park, J.-S., Jin, H., and Nishimura, Y. (2015). Plasmapause location under quiet geomagnetic conditions ($K_p \leq 1$): THEMIS observations. *Res. Lett.* 42, 7303–7310. doi:10.1002/2015GL066690
- Larsen, B. A., Klumpar, D. M., and Gurgiolo, C. (2007). Correlation between plasmapause position and solar wind parameters. *J. Atmos. Solar-Terrestrial Phys.* 69, 334–340. doi:10.1016/j.jastp.2006.06.017
- Lin, D., Wang, W., Merkin, V. G., Huang, C., Oppenheim, M., Sorathia, K., et al. (2022). Origin of dawnside subauroral polarization streams during major geomagnetic storms. *AGU Adv.* 3, e2022AV000708. doi:10.1029/2022AV000708
- Liu, X., and Liu, W. (2014). A new plasmapause location model based on THEMIS observations. *Sci. China Earth Sci.* 57, 2552–2557. doi:10.1007/s11430-014-4844-1
- Liu, X., Liu, W., Cao, J. B., Fu, H. S., Yu, J., and Li, X. (2015). Dynamic plasmapause model based on THEMIS measurements. *J. Geophys. Res. Space Phys.* 120, 10543–10556. doi:10.1002/2015JA021801
- Loi, S. T., Murphy, T., Cairns, I. H., Menk, F. W., Waters, C. L., Erickson, P. J., et al. (2015). Real-time imaging of density ducts between the plasmasphere and ionosphere. *Geophys. Res. Lett.* 42, 3707–3714. doi:10.1002/2015GL063699
- Lyons, L. R., and Thorne, R. M. (1973). Equilibrium structure of radiation belt electrons. *J. Geophys. Res.* 78 (13), 2142–2149. doi:10.1029/JA078i013p02142
- Ma, Q., Li, W., Bortnik, J., Thorne, R. M., Chu, X., Ozeke, L. G., et al. (2018). Quantitative evaluation of radial diffusion and local acceleration processes during GEM challenge events. *J. Geophys. Res. Space Phys.* 123, 1938–1952. doi:10.1002/2017JA025114
- Malaspina, D. M., Jaynes, A. N., Boulé, C., Bortnik, J., Thaller, S. A., Ergun, R. E., et al. (2016). The distribution of plasmaspheric Hiss Wave Power with respect to plasmapause location. *Geophys. Res. Lett.* 43, 7878–7886. doi:10.1002/2016GL069982
- Malaspina, D. M., Jaynes, A. N., Elkington, S., Chan, A., Hospodarsky, G., and Wygant, J. (2020). Testing the organization of lower-band whistler-mode chorus wave properties by plasmapause location. *J. Geophys. Res. Space Phys.* 126, e2020JA028458. doi:10.1029/2020JA028458
- Malaspina, D. M., Ripoll, J.-F., Chu, X., Hospodarsky, G., and Wygant, J. (2018). Variation in plasmaspheric hiss wave power with plasma density. *Geophys. Res. Lett.* 45, doi:10.1029/2018GL078564
- Marchaudon, A., and Bletly, P.-L. (2015). A new interhemispheric 16-moment model of the plasmasphere-ionosphere system: Ipim. *J. Geophys. Res. Space Phys.* 120, 5728–5745. doi:10.1002/2015JA021193
- Marchaudon, A., Bletly, P.-L., Grandin, M., Aikio, A., Kozlovsky, A., and Virtanen, I. (2018). IPIM modeling of the ionospheric F2 layer depletion at high latitudes during a high-speed stream event. *Space Phys. Space Phys.* 123, 7051–7066. doi:10.1029/2018JA025744
- Marchaudon, A., and Bletly, P.-L. (2020). Impact of the dipole tilt angle on the ionospheric plasma as modeled with IPIM. *IPIM. J. Geophys. Res. Space Phys.* 125, e2019JA027672. doi:10.1029/2019JA027672
- Maruyama, N., Sun, Y.-Y., Richards, P. G., Middlecoff, J., Fang, T.-W., Fuller-Rowell, T. J., et al. (2016). A new source of the midlatitude ionospheric peak density structure revealed by a new ionosphere-plasmasphere model. *Geophys. Res. Lett.* 43, 2429–2435. doi:10.1002/2015GL067312
- Matsuda, S., Hasegawa, T., Kumamoto, A., Tsuchiya, F., Kasahara, Y., Miyoshi, Y., et al. (2020). Detection of UHR frequencies by a convolutional neural network from Arase/PWE data. *J. Geophys. Res. Space Physics* 125, e2020JA028075. doi:10.1029/2020JA028075
- Mauk, B. H., Fox, N. J., Kanekal, S. G., Kessel, R. L., Sibeck, D. G., and Ukhorskiy, A. (2013). Science objectives and rationale for the radiation belt storm probes mission. *Space Sci. Rev.* 179 (1–4), 3–27. doi:10.1007/s11214-012-9908-y
- Merkin, V. G., Lyon, J. G., and Claudepierre, S. G. (2013). Kelvin-Helmholtz instability of the magnetospheric boundary in a three-dimensional global MHD simulation during northward IMF conditions. *J. Geophys. Res. Space Phys.* 118, 5478–5496. doi:10.1002/jgra.50520
- Merkin, V. G., and Lyon, J. G. (2010). Effects of the low-latitude ionospheric boundary condition on the global magnetosphere. *J. Geophys. Res.* 115, A10202. doi:10.1029/2010ja015461
- Merkin, V. G., Panov, E. V., Sorathia, K., and Ukhorskiy, A. Y. (2019). Contribution of bursty bulk flows to the global dipolarization of the magnetotail during an isolated substorm. *J. Geophys. Res. Space Phys.* 64, 8647–8668. doi:10.1029/2019ja026872
- Miyoshi, Y., Shinohara, I., Takashima, T., Asamura, K., Higashio, N., Mitani, T., et al. (2018). Geospace exploration project ERG. *Earth Planets Space* 70, 101. doi:10.1186/s40623-018-0862-0
- Moldwin, M. B., Downward, L., Rassoul, H. K., Amin, R., and Anderson, R. R. (2002). A new model of the location of the plasmapause: CRRES results. *J. Geophys. Res.* 107 (11), 1339. doi:10.1029/2001JA009211
- Nsumei, P., Reinisch, B. W., Huang, X., and Bilitza, D. (2012). New Vary-Chap profile of the topside ionosphere electron density distribution for use with the IRI model and the GIRO real time data. *Radio Sci.* 47, RS0L16. doi:10.1029/2012RS004989

- Obana, Y., Maruyama, N., Shinbori, A., Hashimoto, K. K., Fedrizzi, M., Nosé, M., et al. (2019). Response of the ionosphere-plasmasphere coupling to the September 2017 storm: What erodes the plasmasphere so severely? *Space weather*. 17, 861–876. doi:10.1029/2019SW002168
- O'Brien, T. P., and Moldwin, M. B. (2003). Empirical plasmopause models from magnetic indices. *Geophys. Res. Lett.* 30 (4), 2002GL016007. doi:10.1029/2002GL016007
- Ozhogin, P., Tu, J., Song, P., and Reinisch, B. W. (2012). Field-aligned distribution of the plasmaspheric electron density: An empirical model derived from the IMAGE RPI measurements. *J. Geophys. Res.* 117, A06225. doi:10.1029/2011JA017330
- Pembroke, A., Toffoletto, F., Sazykin, S., Wiltberger, M., Lyon, J., Merkin, V., et al. (2012). Initial results from a dynamic coupled magnetosphere-ionosphere-ring current model. *J. Geophys. Res.* 117, A02211. doi:10.1029/2011JA016979
- Pham, K., Zhang, B., Sorathia, K., Dang, T., Wang, W., Merkin, V., et al. (2021). Thermospheric density perturbations produced by traveling atmospheric disturbances during August 2005 Storm. *Earth Space Sci. Open Archive* 19, 10508477. doi:10.1002/essoar.10508477.1
- Pierrard, V., Botek, E., and Darrouzet, F. (2021b). Improving predictions of the 3D dynamic model of the plasmasphere. *Front. Astron. Space Sci.* 8, 69681401. doi:10.3389/fspas.2021.681401
- Pierrard, V., Botek, E., Ripoll, J.-F., Thaller, S. A., Moldwin, M. B., Ruohoniemi, M., et al. (2021c). Links of the plasmopause with other boundary layers of the magnetosphere: Ionospheric convection, radiation belt boundaries, auroral oval. *Auror. Oval. Front. Astron. Space Sci.* 8, 728531. doi:10.3389/fspas.2021.728531
- Pierrard, V., Goldstein, J., André, N., Jordanova, V. K., Kotova, G. A., Lemaire, J. F., et al. (2009). Recent progress in physics-based models of the plasmasphere. *Space Sci. Rev.* 145, 193–229. doi:10.1007/s11214-008-9480-7
- Pierrard, V., and Lemaire, J. (2004). Development of shoulders and plumes in the frame of the interchange instability mechanism for plasmopause formation. *Geophys. Res. Lett.* 31 (5), L05809–L05811. doi:10.1029/2003GL018919
- Pierrard, V., and Lemaire, J. (2001). Exospheric model of the plasmasphere. *J. Atmos. Solar-Terrestrial Phys.* 63 (11), 1261–1265. doi:10.1016/s1364-6826(00)00227-3
- Pierrard, V., Ripoll, J.-F., Cunningham, G., Botek, E., Santolik, O., Thaller, S., et al. (2021a). Observations and simulations of dropout events and flux enhancements in October 2013: Comparing MEO equatorial with LEO polar orbit. *J. Geophys. Res. Space Phys.* 126, e2020JA028850. doi:10.1029/2020JA028850
- Pierrard, V., and Stegen, K. (2008). A three dimensional dynamic kinetic model of the plasmasphere. *J. Geophys. Res. Space Phys.* 113, A10209. doi:10.1029/2008ja013060
- Pierrard, V., and Voiculescu, M. (2011). The 3D model of the plasmasphere coupled to the ionosphere. *Geophys. Res. Lett.* 38, L12104. doi:10.1029/2011GL047767
- Raissi, M., Perdikaris, P., and Karniadakis, G. E. (2019). Physics-informed neural networks: A deep learning framework for solving forward and inverse problems involving nonlinear partial differential equations. *J. Comput. Phys.* 378, 686–707. doi:10.1016/j.jcp.2018.10.045
- Reinisch, B. W., Huang, X., Song, P., Green, J. L., Fung, S. F., Vasyliunas, V. M., et al. (2004). Plasmaspheric mass loss and refilling as a result of a magnetic storm. *J. Geophys. Res.* 109, A01202. doi:10.1029/2003JA009948
- Reinisch, B. W., Nsumei, P., Huang, X., and Bilitza, D. K. (2007). Modeling the F2 topside and plasmasphere for IRI using IMAGE/RPI, and ISIS data. *Adv. Space Res.* 39, 731–738. doi:10.1016/j.asr.2006.05.032
- Richards, P. G., Meier, R. R., and Wilkinson, P. J. (2010). On the consistency of satellite measurements of thermospheric composition and solar EUV irradiance with Australian ionosonde electron density data. *J. Geophys. Res.* 115, A10309. doi:10.1029/2010JA015368
- Richmond, A. D. (1995). Ionospheric electrodynamic using magnetic apex coordinates. *J. Geomagn. Geoelectr.* 47, 191–212. doi:10.5636/jgg.47.191
- Ripoll, J.-F., Claudepierre, S. G., Ukhorskiy, A. Y., Colpitts, C., Li, X., Fennell, J., et al. (2020a). Particle dynamics in the Earth's radiation belts: Review of current research and open questions. *J. Geophys. Res. Space Phys.* 125, e2019JA026735. doi:10.1029/2019JA026735
- Ripoll, J.-F., Denton, M. H., Hartley, D. P., Reeves, G. D., Malaspina, D., Cunningham, G. S., et al. (2020b). Scattering by whistler-mode waves during a quiet period perturbed by substorm activity. *J. Atmos. Solar-Terrestrial Phys.* 215, 105471. doi:10.1016/j.jastp.2020.105471
- Ripoll, J.-F., Kluth, G., Has, S., Fischer, A., Mougeot, M., and Camporeale, E. (2022b). "Exploring pitch-angle diffusion during high speed streams with neural networks," in 2022 3rd URSI Atlantic and Asia Pacific Radio Science Meeting (AT-AP-RASC), Gran Canaria, Spain, 2022, 1–4. doi:10.23919/AT-APRASC54737.2022.9814235
- Ripoll, J.-F., Loridan, V., Denton, M. H., Cunningham, G., Reeves, G., Santolik, O., et al. (2019). Observations and Fokker-Planck simulations of the L-shell, energy, and pitch angle structure of Earth's electron radiation belts during quiet times. *J. Geophys. Res. Space Phys.* 124, 1125–1142. doi:10.1029/2018ja026111
- Ripoll, J.-F., Reeves, G. D., Cunningham, G. S., Loridan, V., Denton, M., Santolik, O., et al. (2016). Reproducing the observed energy dependent structure of Earth's electron radiation belts during storm recovery with an event-specific diffusion model. *Geophys. Res. Lett.* 43, 5616–5625. doi:10.1002/2016GL068869
- Ripoll, J.-F., Santolik, O., Reeves, G. D., Kurth, W. S., Denton, M. H., Loridan, V., et al. (2017). Effects of whistler mode hiss waves in March 2013. *J. Geophys. Res. Space Phys.* 122, 7433–7462. doi:10.1002/2017JA024139
- Ripoll, J.-F., Thaller, S. A., Hartley, D. P., Cunningham, G. S., Pierrard, V., Kurth, W. S., et al. (2022a). Statistics and empirical models of the plasmasphere boundaries from the van allen probes for radiation belt physics. *Geophys. Res. Lett.* 49, e2022GL101402. doi:10.1029/2022GL101402
- Saikin, A. A., Shprits, Y. Y., Drozdov, A. Y., Landis, D. A., Zhelavskaya, I. S., and Cervantes, S. (2021). Reconstruction of the radiation belts for solar cycles 17–24 (1933–2017). *Space weather*. 19, e2020SW002524. doi:10.1029/2020SW002524
- Sheeley, B. W., Moldwin, M. B., Rassoul, H. K., and Anderson, R. R. (2001). An empirical plasmasphere and trough density model: CRRES observations. *J. Geophys. Res.* 106 (11), 25631. doi:10.1029/2000JA000286
- Shprits, Y., Subbotin, D., Drozdov, A., Usanova, M. E., Kellerman, A., Orlova, K., et al. (2013). Unusual stable trapping of the ultrarelativistic electrons in the Van Allen radiation belts. *Nat. Phys.* 9, 699–703. doi:10.1038/nphys2760
- Singh, A. K., Singh, R. P., and Siingh, D. (2011). State studies of Earth's plasmasphere: A review. *Planet. Space Sci.* 59, 810–834. doi:10.1016/j.pss.2011.03.013
- Sorathia, K. A., Michael, A., Merkin, V., Ukhorskiy, A., Turner, D. L., Lyon, J., et al. (2021). The role of mesoscale plasma sheet dynamics in ring current formation. *Front. Astron. Space Sci.* 8, 761875. doi:10.3389/fspas.2021.761875
- Sorathia, K. A., Merkin, V. G., Panov, E. V., Zhang, B., Lyon, J. G., Garretson, J., et al. (2020). Ballooning-interchange instability in the near-earth plasma sheet and auroral beads: Global magnetospheric modeling at the limit of the MHD approximation. *Geophys. Res. Lett.* 47, e2020GL088227. doi:10.1029/2020gl088227
- Sorathia, K. A., Ukhorskiy, A. Y., Merkin, V. G., Fennell, J. F., and Claudepierre, S. G. (2018). Modeling the depletion and recovery of the outer radiation belt during a geomagnetic storm: Combined MHD and test particle simulations. *J. Geophys. Res. Space Phys.* 123, 5590–5609. doi:10.1029/2018ja025506
- Storey, L. R. O. (1953). An investigation of whistling atmospherics. *Math. Phys. Sci.* 246, 246113–246141. doi:10.1098/rsta.1953.0011
- Subbotin, D. A., and Shprits, Y. Y. (2009). Three-dimensional modeling of the radiation belts using the Versatile Electron Radiation Belt (VERB) code. *Space weather*. 7, S10001. doi:10.1029/2008SW000452
- Sun, Y.-Y., Matsuo, T., Maruyama, N., and Liu, J.-Y. (2015). Field-aligned neutral wind bias correction scheme for global ionospheric modeling at midlatitudes by assimilating FORMOSAT-3/COSMIC $\langle scp \rangle$ $\langle i \rangle$ $\langle h \rangle$ $\langle sub \rangle$ $\langle m \rangle$ $\langle /sub \rangle$ $\langle F \rangle$ $\langle lscp \rangle$ $\langle /i \rangle$ $\langle 2 \rangle$ data under geomagnetically quiet conditions. *J. Geophys. Res. Space Phys.* 120, 3130–3149. doi:10.1002/2014JA020768
- Tapping, K. F. (2013). The 10.7 cm solar radio flux (F10.7). *Space weather*. 11, 394–406. doi:10.1002/swe.20064
- Thaller, S., Ripoll, J.-F., Nishimura, T., and Erickson, P. (2022). Editorial: Coupled feedback mechanisms in the magnetosphere-ionosphere system. *Front. Astron. Space Sci.* 9, 1011217. doi:10.3389/fspas.2022.1011217
- Thomas, N., Shiokawa, K., Miyoshi, Y., Kasahara, Y., Shinohara, I., Kumamoto, A., et al. (2021). Investigation of small-scale electron density irregularities observed by the Arase and Van Allen Probes satellites inside and outside the plasmasphere. *J. Geophys. Res. Space Phys.* 126, e2020JA027917. doi:10.1029/2020JA027917
- Thorne, R. M. (2010). Radiation belt dynamics: The importance of wave-particle interactions. *Geophys. Res. Lett.* 37, L22107. doi:10.1029/2010GL044990
- Toffoletto, F., Sazykin, S., Spiro, R., and Wolf, R. (2003). Inner magnetospheric modeling with the rice convection model. *Space Sci. Rev.* 107, 175–196. doi:10.1023/a:1025532008047
- Torkar, K., Nakamura, R., Wellenzohn, S., Jeszenszky, H., Torbert, R. B., Lindqvist, P. A., et al. (2019). Improved determination of plasma density based on spacecraft potential of the magnetospheric Multiscale mission under active potential control. *IEEE Trans. Plasma Sci.* 47 (8), 3636–3647. doi:10.1109/TPS.2019.2911425
- Torkar, K., Nakamura, R., Tajmar, M., Scharlemann, C., Jeszenszky, H., Laky, G., et al. (2016). Active spacecraft potential control investigation. *Space Sci. Rev.* 199, 515–544. doi:10.1007/s11214-014-0049-3
- Tu, W., Cunningham, G. S., Chen, Y., Henderson, M. G., Camporeale, E., and Reeves, G. D. (2013). Modeling radiation belt electron dynamics during GEM challenge intervals with the DREAM3D diffusion model. *J. Geophys. Res. Space Phys.* 118, 6197–6211. doi:10.1002/jgra.50560
- Tu, W., Li, X., Chen, Y., Reeves, G. D., and Temerin, M. (2009). Storm-dependent radiation belt electron dynamics. *J. Geophys. Res.* 114 (2), A02217. doi:10.1029/2008JA013480
- Verbanac, G., Pierrard, V., Bandić, M., Darrouzet, F., Rauch, J.-L., and Décréau, P. (2015). The relationship between plasmopause, solar wind and geomagnetic activity between 2007 and 2011. *Ann. Geophys.* 33, 1271–1283. doi:10.5194/angeo-33-1271-2015
- Wang, D., and Shprits, Y. Y. (2019). On how high-latitude chorus waves tip the balance between acceleration and loss of relativistic electrons. *Geophys. Res. Lett.* 46, 7945–7954. doi:10.1029/2019GL082681
- Wang, Y., Tu, J., and Song, P. (2015). A new dynamic fluid-kinetic model for plasma transport within the plasmasphere. *J. Geophys. Res.* 120, 8486–8502. doi:10.1002/2015ja021345
- Wygant, J. R., Bonnell, J. W., Goetz, K., Ergun, R. E., Mozer, F. S., Bale, S. D., et al. (2013). The electric field and waves instruments on the radiation belt storm probes mission. *Space Sci. Rev.* 179 (1–4), 183–220. doi:10.1007/s11214-013-0013-7

- Zhang, B., Brambles, O. J., Cassak, P. A., Ouellette, J. E., Wiltberger, M., Lotko, W., et al. (2017). Transition from global to local control of dayside reconnection from ionospheric-sourced mass loading. *J. Geophys. Res. Space Phys.* 122, 9474–9488. doi:10.1002/2016ja023646
- Zhang, B., Sorathia, K. A., Lyon, J. G., Merkin, V. G., Garretson, J. S., and Wiltberger, M. (2019). Gamera: A three-dimensional finite-volume MHD solver for non-orthogonal curvilinear geometries. *Astrophys. J. Suppl. Ser.* 244 (1), 20.
- Zhelavskaya, I. S., Aseev, N. A., and Shprits, Y. Y. (2021). A combined neural network- and physics-based approach for modeling plasmasphere dynamics. *J. Geophys. Res. Space Phys.* 126, e2020JA028077. doi:10.1029/2020JA028077
- Zhelavskaya, I., Shprits, Y., Spasojevic, M., and Kurth, W. (2020). Electron density derived with the neural-network-based upper-hybrid resonance determination algorithm from the van allen probes EMFISIS measurements. *GFZ Data Serv.* 2020, 245. doi:10.5880/GFZ.2.8.2020.002
- Zhelavskaya, I. S., Shprits, Y. Y., and Spasojevic, M. (2017). Empirical modeling of the plasmasphere dynamics using neural networks. *J. Geophys. Res. Space Phys.* 122, 11227–11244. doi:10.1002/2017JA024406
- Zhelavskaya, I. S., Shprits, Y. Y., and Spasojevic, M. (2018). “Reconstruction of plasma electron density from satellite measurements via artificial neural networks,” in *Machine learning techniques for space weather*. Editors E. Camporeale and S. J. R. WingJohnson (Netherlands: Elsevier), 301–327. doi:10.1016/B978-0-12-811788-0.00012-3
- Zhelavskaya, I. S., Spasojevic, M., Shprits, Y. Y., and Kurth, W. S. (2016). Automated determination of electron density from electric field measurements on the Van Allen Probes spacecraft. *J. Geophys. Res. Space Phys.* 121, 4611–4625. doi:10.1002/2015JA022132